March 8th, 2026

A kinematic equation for the morphogenetic reproducibility of an animal

Jianguo Wang[1, #], Long Xiao[2, #], Miaoling Yang[2], Zeqi Yao[1], Shanjun Deng[1], Zhuo Du[2] & Xionglei He[1]

[1] Hongkong Institute for Advanced Studies, School of Life Sciences, Sun Yat-sen University, Guangzhou 510275, China

[2] State Key Laboratory of Molecular Developmental Biology, Institute of Genetics and Developmental Biology, Chinese Academy of Sciences, Beijing 100101, China

[#] These authors contribute equally

Correspondence should be addressed to:

X.H. (hexiongl@mail.sysu.edu.cn) or Z.D. (zdu@genetics.ac.cn)

One-sentence Summary: How cell positioning is regulated in embryos to achieve reproducible morphogenesis, a question that has long fascinated both biologists and physicists, is now answered by a golden-ratio-parameterized cell kinematic equation in the nematode *C. elegans*.

Abstract

It is intriguing how cell positioning is regulated during animal development to achieve reproducible morphogenesis under genetic or environmental perturbations. In this study, we track single-cell spatiotemporal dynamics in over 2,000 *C. elegans* embryos subjected to diverse perturbations. By analyzing the inheritance of cell position along developmental lineages, we uncover ubiquitous negative-feedback "canals" that prevent the propagation of positional noise, thereby ensuring morphogenetic reproducibility. Examining cell kinematic parameters reveals that cell migration velocity underlies the negative-feedback regulation. The velocity dynamics

across cell generations are described by a self-similar equation characterized by a single parameter φ (the golden ratio) that quantifies velocity adjustment, suggesting an inherent program recurrently employed by cells to attain their expected positions. Further analysis shows that φ = 0.618 represents the theoretical optimum, enabling an expected zero net noise accumulation and thus along-lineage conservation of cell velocity. Deviation from this self-similar equation predicts hatching failure (AUC = 0.89), and reveals a set of cytoskeleton-enriched genes required for its maintenance. In summary, by revealing a conservation principle of cell kinematics in *C. elegans* embryos, this study establishes a novel kinematic-mechanical framework for investigating animal morphogenesis, highlighting a golden-ratio-embedded natural design adaptable to general dynamic systems for noise control.

Introduction

Animal morphogenesis requires delicate regulation of cell positioning during development. Although the programs setting where, when and how a cell originates, migrates and divides in an embryo can be highly precise, fluctuations arising from genetic, environmental and stochastic factors unavoidably introduce noises, deviations from the expected settings, into each decision. Because development is a time series process in an expanding cell population, such noises could quickly accumulate along lineages over time and become non-negligible at the end of development, undermining the phenotypic reproducibility of the end-products. Hence, biologists have long been fascinated by the extraordinary reproducibility of developmental end-products observed in multicellular organisms, in particular, animals[1,2]. In the seminal 1942 paper[3], Waddington wrote, "…*developmental reactions are in general canalized. That is to say, they are adjusted so as to bring about one definite end-result regardless of minor variations in conditions during the course of the reaction*." Since then, canalization has become a central concept in biology, motivating numerous studies on the control of molecular noise at the cellular level (e.g., Hsp90 for protein-folding noise suppression) [4-7]. However, intracellular noise-control mechanisms do not resolve the problem of cell behavioral noise at the embryonic level. The developmental "canals" constituting Waddington's canalization landscape, which prevent the propagation of cell behavioral noise along developmental lineages within an embryo, have not been characterized in any organism. In recent years, mechanical and geometric approaches have emerged as powerful

frameworks for uncovering the systematic principles of embryogenesis, organogenesis, and tissue patterning[1,8-29], yet these studies have largely focused on cells' expected states or their collective behaviors during morphogenesis rather than on the control of cell behavioral noises at the embryonic level. Consequently, although embryonic canalization, or developmental reproducibility, has been examined from multiple perspectives[11,12,15,16,21,26,30-40] in qualitative or coarse-grained ways, it remains unresolved whether a direct quantitative mechanism governs single-cell-resolution noise control of cell behavior to ensure developmental reproducibility at the embryonic level.

A prerequisite for quantifying such cell noise control is systematic tracing cell behaviors throughout development under various conditions and aligning different embryos into a common geometric representation system, a challenging task in most multicellular organisms. The nematode *C. elegans* is ideal for this purpose due to its fully mapped, invariant cell lineage and the availability of single-cell phenotypic tracing methods[41-47]. During *C. elegans* embryogenesis, each individual follows an invariant cell lineage to produce a fixed number of cells each with a defined function[41]. The developmental stereotype enables the comparison of matched cells between individuals to quantify the expected cell behaviors as well as the cell behavior noises in a specific individual. In previous studies, we and others have characterized cell behaviors regarding cell morphology, mechanics, proliferation, differentiation, and morphogenesis in a variety of *C. elegans* embryos[32,38,42,43,46,48-54], and observed widespread noise-buffering events[32,38,50,52,53]. However, the mechanisms that suppress the noise propagation along cell lineages to ensure developmental reproducibility remain poorly understood. In particular, it remains unclear whether a unified mathematical-physical principle governs the dynamics of cell-behavioral noise during development.

In this study, we used time-lapse microscopy to track *C. elegans* morphogenesis and analyzed over 2,000 embryos subjected to diverse genetic and environmental perturbations. Lineage-resolved spatiotemporal features, including cell position and cell cycle length, were recorded for every tracked cell in each embryo. By modeling the transmission of cell positional noise, we uncovered comprehensive negative-feedback "canals" that prevent noise propagation along cell lineages. Through quantitative analysis of cell kinematics, we further revealed the mechanical basis of this negative feedback as the regulation of cell migration velocity. Strikingly,

we found that cell velocity dynamics follow a self-similar equation with a single parameter - the golden ratio (φ = 0.618), which emerges as a mathematical optimum satisfying a velocity conservation principle. Under this principle, noise generated in any cell is precisely counteracted by continuous suppression accumulated along its lineage, resulting in an expected zero net noise. Theoretical analysis demonstrates the mathematical optimality, robustness to perturbations, evolutionary achievability, and biological feasibility of the φ-parameterized self-similar equation. Moreover, the equation explains embryonic hatching lethality as a consequence of its violation, identifies a set of cytoskeleton-enriched genes required for its maintenance, and provides a unifying framework linking mother–daughter negative feedback with the long-standing mother–sister similarity paradox. Together, these results provide the first quantitative characterization of Waddington's canalization landscape, revealing an elegant golden-ratio-embedded conservation principle of cell kinematics for securing morphogenetic reproducibility in *C. elegans*.

Results

Tracking cell spatiotemporal information during *C. elegans* embryogenesis

As in our recent study[32], we used time-lapse microscopic imaging to track the embryogenesis of *C. elegans* (**Methods**). In brief, the ubiquitously expressed histone::mCHerry fluorescence protein was used to label individual cells to achieve single-cell-resolution tracking of the nematode embryogenesis from the 4-cell stage up to the 350-cell stage, which corresponds to the completion of nine rounds of cell division (out of ten in total). The spatiotemporal features were recorded for all individual cells that appear within the tracked time window (**Fig. 1a; Methods**). Specifically, the time-lapse three-dimensional positions (x, y and z coordinates) of the cells were obtained; meanwhile, the cell division timing was available for every cell, with which cell cycle length (CCL) can be readily derived from the time interval between two consecutive cell divisions.

To mimic environmental perturbations, we exposed wild-type *C. elegans* embryos to 40 different stress conditions of eight types of stressors (temperature, heat shock, bacterial food, stearic acid, glucose, NaCl, $FeCl_3$, and paraquat) (**Methods**). In total, we tracked 111 environmentally perturbed embryos (hereafter called Env embryos), and obtained the aforementioned cellular features. To examine the effect of genetic perturbations, we included

1,823 embryos (hereafter called RNAi embryos) that were cultured under normal environment but each subjected to single-gene RNAi knockdown (with ~700 different genes involved). The embryogenesis of these RNAi embryos was tracked by our recent study with the same imaging protocol[32]. In addition, the embryogenesis data of 105 control embryos with neither environmental nor genetic perturbations were also included[32]. Taken together, a total of 2,039 embryos were examined in this study (**Fig. 1a and Table S1-S3**).

Considering that some embryos had unusual global sizes or CCLs, we normalized the raw cell feature values across different embryos to enhance comparability[44,46]. To do so, for CCL we linearly aligned each embryo to a randomly selected reference control embryo (ctr-emb58) to derive embryo-specific scaling factors (**Fig. S1; Methods**); the raw CCL values of an embryo were then all divided by the embryo-specific scaling factor to obtain the scaled CCL values of the embryo. For cell position, each embryo was first translated and rotated such that they had matched x, y and z coordinates, with the gravity center of all cells at the point of origin (i.e., gravity center has x = 0, y = 0, z = 0) (**Fig. 1b and Fig. S2; Methods**). Then, with the same procedure as for scaling CCLs, each embryo was aligned to the reference embryo (ctr-emb58) to obtain the scaled 3D position values (x, y and z) (**Fig. S2; Methods**). The scaling was not sensitive to the choice of reference because the scaling factors obtained based on ctr-emb58 were highly correlated to those based on the average of all control embryos (Pearson' R > 0.999 for CCL, x-coordinate and y-coordinate, and = 0.984 for z-coordinate; **Fig. S1-S2**). Unless otherwise stated, all following analyses in this study were based on the scaled cell feature values.

Modeling mother-daughter cell noise transmission

Because the developmental cell lineages of *C. elegans* are stereotyped, it is biologically meaningful to compare cells of the same lineage identity in different embryos[41,43]. We focused on the three-dimensional positions (i.e., *x*, *y* and *z* coordinates) of each cell in the embryos. Notably, considering the *x*, *y* and *z* coordinates separately facilitated the definition of both the magnitude and the direction of cell positional noise. For a given cell there were often substantial position variabilities observed among the embryos; the average position was regarded as the expected position of the cell and the deviation from the average was regarded as noise (**Fig. 1c and Fig. S3**).

Using the x-coordinate position as an example, we modeled the position of a daughter cell (x_{D}) with that of its mother cell (x_{M}) by an ordinary linear regression:

$$x_{\mathrm{D}} = ax_{\mathrm{M}} + b + \varepsilon, \quad (1)$$

where a, b and ε represent the slope, intercept and residual term, respectively. This model aligns with previous studies on noise transmission along bacteria or yeast cell lineages[55,56]. Eq. (1) is equivalent to $x_{\mathrm{D}} - \overline{x_{\mathrm{D}}} = a(x_{\mathrm{M}} - \overline{x_{\mathrm{M}}}) + \varepsilon$, where $\overline{x_{\mathrm{D}}}$ represents the mean x-coordinate position of the daughter among all embryos, $\overline{x_{\mathrm{M}}}$ represents that of the mother, and $b = \overline{x_{\mathrm{D}}} - a\overline{x_{\mathrm{M}}}$. As such, $x_{\mathrm{D}} - \overline{x_{\mathrm{D}}}$ and $x_{\mathrm{M}} - \overline{x_{\mathrm{M}}}$ signify the x-coordinate noise of the daughter and the mother, respectively. Hence, as in previous studies[55,56], the noise we here defined referred to deviation from the mean of all examined embryos. The noise transmission model can then be written as:

$$\Delta X = kX_{\mathrm{M}} + \varepsilon, \quad (2)$$

where $X_{\mathrm{M}} = x_{\mathrm{M}} - \overline{x_{\mathrm{M}}}$ and $X_{\mathrm{D}} = x_{\mathrm{D}} - \overline{x_{\mathrm{D}}}$ represent the noise of the mother and the daughter, respectively, $\Delta X = X_{\mathrm{D}} - X_{\mathrm{M}}$ represents the noise difference of the daughter from its mother, and ε is the same as that in Eq. (1). Notably, the slope k in Eq. (2) is equal to a -1, where a is the slope in Eq. (1).

As shown in **Fig. 1d**, the direction of k defines three possible scenarios: Because the position of a cell is based on its preceding position, $k = 0$ means no feedback is involved such that the daughter fully inherits the positional noise of its mother; $k < 0$ means negative feedback wherein only a fraction of the mother's noise is transmitted to the daughter; and $k > 0$ means positive feedback wherein the noise of the daughter is enhanced relative to that of its mother. The weakening or enhancing of cell noise here refers to the variance of noise instead of the absolute noise level that is also influenced by ε. Notably, the three scenarios lead to distinct noise accumulation patterns along developmental lineages, serving as a general criterion for time-series system stability[55,56].

Discovery of negative-feedback canals for preventing positional noise propagation

We first looked at ABal-ABala, a randomly selected mother-daughter (M-D) cell pair with ABal being the mother cell and ABala the daughter. **Fig. 2a** shows the x-coordinate positional noise of ABal (i.e., X_{ABal}) versus the daughter-mother noise difference ($\Delta X = X_{\mathrm{ABala}} - X_{\mathrm{ABal}}$) in each of the

2,039 embryos, with k = -0.68 observed. The result suggests a negative-feedback regulation on the daughter's noise by referring to the mother's noise. In other words, the mother's noise was transmitted to the daughter but with a mother-dependent offset (i.e., kX_M). Notably, $k = 0$ implies full noise transmission from mother to daughter while k = -1 indicates complete negative feedback with no net noise transmitted from mother to daughter. Here, the observed k = -0.68 means a strong but incomplete negative-feedback effect.

To have a general picture we examined all M-D cell pairs at three coordinates, respectively. The observed k was nearly all negative with a strong statistical support (**Fig. 2b, Fig. S4 and Table S4)**, with only four cell pairs being exceptions at the y-coordinate (median k_x = -0.61, k_y = -0.66, and k_z = -0.74). The k values varied across generations and peaked in the middle developmental stages (**Fig. 2c and Fig. S4**), showing an hourglass pattern which suggests a correspondence between weaker developmental canalization and higher evolutionary conservation at the middle-stage of embryogenesis[57]. Comparing the k values at three coordinates and three types of embryos (control, RNAi and Env) showed strong correlations between the coordinates (**Fig. S4**) and the embryo types (**Fig. S4**). When shuffling the cells to create pseudo M-D cell pairs, we failed to find such negative feedbacks with weakly positive M-D correlations that are expected for partial noise transmission in real M-D pairs (**Fig. 2d and Fig. S4; Methods**). The results remained robust after considering several confounding factors including the 'dilution effect' (i.e., regression to the mean) due to measurement error, scaling factor distribution, alignment quality, lineage tracing accuracy, mother-daughter standard deviation ratio, and alignment procedure (**Fig. S5-S10; Methods**). Additionally, the negative-feedback effect did not depend on cell stage choice; when analyzing both the birth and division stages of a cell, we found consistent negative feedback across stages and accumulated negative feedback over time (**Fig. S11**).

The ubiquitous M-D negative feedbacks were remarkable because they were concatenated along each lineage to form continuous 'canals'. As in **Fig. 2e,** from ABal to ABalpppp the five M-D negative feedbacks together formed such a canal to stabilize the cell positions along this lineage. All these continuous 'canals' therefore together characterized the Waddington's canalization landscape which served as an effective 'design' for preventing noise propagation during the development. Importantly, it is an inherent mathematical property that a continuous negative-feedback canal is competent in preventing noise propagation, because the noise accumulation curve quickly reaches a plateau while positive feedback or no feedback would lead

to continuous noise propagation (**Fig. 2f and Supplementary Note I**; **Methods**). Thus, Waddington's developmental canals were no longer just a metaphor but were mathematically formulated, with the estimated *k* serving as a quantitative measure of noise suppression efficacy.

To further demonstrate the efficacy of the canals we simulated a scenario without such canals. In that scenario, $k = 0$ and the noise of a daughter cell would comprise two parts: one inherited fully from its mother and the other representing the mother-independent noise arising independently from its mother. As a consequence, cell noise would accumulate constantly along a cell lineage by adding up the initial mother cell noise and all subsequent mother-independent noises. We estimated the expected cell noise accumulation without negative feedbacks (i.e., $k = 0$) (**Methods**). Due to incomplete data for earlier cells, we considered the eight cells of the 4^{th} generation as the initial mother cells of the lineages. **Fig. 2g** shows the observed and expected noise accumulations along eight representative lineages. On average, the expected noise variance among embryos was 5.8, 6.6, and 7.7 times the observed noise variance for cells of the 10^{th} generation at the x, y, and z coordinates, respectively (**Fig. 2g and Fig. S12**). Accordingly, under the scenario of no negative feedbacks the cells would gradually deviate from their pre-determined positions, resulting in morphologically abnormal embryos as shown in **Fig. 2h** (**Methods**).

The positional negative feedback is achieved by adjusting cell migration velocity

An M-D negative feedback in cell position can be regarded as the adjustment of migration displacement relative to what would have occurred without such a feedback. As in **Fig. 3a**, reduced migration displacement can result from reduced migration velocity and/or migration time because displacement = velocity × time. Accordingly, there are three possible mechanisms underlying displacement regulation, labeled as γ, τ, and η in **Fig. 3b**. The isovelocity curves (γ) exhibit a parallel time-position pattern (**Fig. 3c**), while the isochronous curves (τ) show a convergent time-position pattern (**Fig. 3d**).

For each M-D cell pair in each embryo, we obtained the position when the mother cell divides, as well as the migration displacement, velocity, and time (i.e., cell cycle length) of the daughter cell (**Methods**). **Fig. 3e** shows the data of an example cell pair Caap-Caapp, in which the position when Caap divides, designated as start position, was negatively correlated with the migration displacement of Caapp, a pattern consistent with the negative feedback observed in **Fig.**

2a. Importantly, start position showed little correlation with migration time (**Fig. 3f**), but a strong negative correlation with migration velocity (**Fig. 3g**). The results were largely the same for other M-D cell pairs (**Fig. 3h** and **Fig. S13**). Hence, the negative feedback in adjusting cell position/displacement was achieved by regulating cell migration velocity but not migration time (cell cycle length). To further demonstrate the point, **Fig. 3i** shows the migration pattern of Caap-Caapp in three embryos, which resembled the isochronous curves depicted in **Fig. 3d**. In addition, although displacement and velocity as directional vectors were considered here, which is appropriate for migration analysis, we found consistent results when distance and speed as scalar metrics were considered **(Fig. S13; Methods**).

The observation that migration displacement was explained by velocity but not time was intriguing. A close examination of the data shows that the CV of migration time was much smaller than that of velocity and that of displacement. This suggests a special developmental design: The cell cycle length (migration time) is tightly controlled to have a very small variability, which makes efficient regulations of displacement via velocity possible (**Supplementary Note II**).

A golden-ratio-embedded self-similar equation reveals the rule of velocity regulation

To better understand how cell velocity is regulated, we plotted its dynamics along each lineage. The velocity was standardized into Z-score to become comparable across cells of different generations (**Methods**). As such, any non-zero velocities mean velocity deviations from the expected settings. As illustrated by a representative embryo (UNC-75_emb2) (**Fig. 4a**), there are clear inter-generational velocity oscillations along each of the lineages, with mostly M- and W-shaped patterns (corresponding to one-generation sign reversal by negative feedback). Similar results were observed for other embryos (**Fig. S14**). To digest the dynamic patterns, we performed an along-lineage autocorrelation analysis within each embryo. Specifically, the correlation (R_t) was computed by comparing each cell's velocity with that of its daughters ($t = 1$), granddaughters ($t = 2$), and more distant progenies, respectively (**Methods**). In nearly all embryos the computed R_1 was negative and remained even after considering position information as a confounding factor (**Fig. S14**). Meanwhile, the proportion of negative R decreased exponentially with increasing t (**Fig. 4b; Methods**), suggesting a gradual decay of negative feedback along developmental lineages.

We hypothesized that the gradual decay might be explained by a self-similar process in which ancestral deviations are progressively corrected in an exponentially decaying manner. To formalize this idea, we adapted the classical geometric distributed lag (GDL) model which has been a fundamental framework for modeling time-series accumulative effects[58]. Specifically, we modeled velocity dynamics by assuming the velocity-determining factor inherited from an ancestor decays geometrically at a constant per-generation rate β, with a common negative-feedback strength α acting on the inherited component. As such, for an initial cell with velocity V, the expected velocity was $-\alpha\beta V$ for its daughters, $-\alpha\beta^2 V$ for its granddaughters, and $-\alpha\beta^n V$ for its n^{th}-generation descendants (**Fig. 4c**). Then, when considering the accumulative effects from all ancestors, the velocity of a cell at generation t (V_t) can be written as:

$$V_t = -\alpha \sum_{i=1}^{t-1} \beta^i V_{t-i} + \varepsilon, \quad (3)$$

where V_{t-i} is the velocity of its ancestor at generation t-i, and ε represents residue term. Because here velocity was standardized, no intercept was included. Exploiting the geometric decay property, this model can be approximated by a three-generation form: $V_t = -\alpha\beta V_{t-1} - \alpha\beta^2 V_{t-2} + \varepsilon$. Using all three-generation trios of the 105 control embryos, we first fitted the ordinary linear model $V_t = -\theta_1 V_{t-1} - \theta_2 V_{t-2} + \varepsilon$ for the x-coordinate velocity (**Methods**), and found θ_1 and θ_2 approximately -0.382 and -0.236, respectively. These numbers were inspiring because, given $\theta_1 = \alpha\beta$ and $\theta_1 = \alpha\beta^2$, they suggested $\alpha \approx \beta \approx 0.618$, the golden ratio conjugate φ (hereafter referred to as the golden ratio) (**Fig. 4d**). Nonlinear regression with the constraint $\alpha = \beta$ produced nearly identical estimates at all three coordinates ($\varphi_x = 0.620\pm0.002$; $\varphi_y = 0.611\pm0.002$; $\varphi_z = 0.626\pm0.002$; $\varphi = 0.619\pm0.001$ when x, y and z combined; mean±s.e.) (**Fig. 4e**), and predictions from the linear and nonlinear models were highly concordant (**Fig. 4f**). These results indicated the cell velocity oscillations along developmental lineages can be described by a one-parameter self-similar equation written as: $V_t = -\varphi \sum_{i=1}^{t-1} \varphi^i V_{t-i} + \varepsilon$, wherein $\varphi = 0.618$.

The golden ratio embedded in the equation could be just a coincidental numerical fit or could represent a natural emergence 'design'. To evaluate this, one can think of a multi-generation cell lineage with an initial velocity deviation. As in **Fig. 4c**, the corresponding negative-feedback strength would be $-\alpha\beta$ at the daughter, $-\alpha\beta^2$ at the granddaughter, and $-\alpha\beta^n$ at the n^{th}-generation descendant. Remarkably, the cumulative negative-feedback strength $-\alpha\beta - \alpha\beta^2 - \ldots - \alpha\beta^n =$

$-\alpha \sum_{i=1}^{n} \beta^i$ would, as in Eq. (4), converge to -1 when $\alpha = \beta = \varphi$ (0.618), which indicates complete counteraction of the initial deviation (or conservation of total velocity along a lineage).

$$\lim_{n\to\infty} (-\alpha \sum_{i=1}^{n} \beta^i) = -1 \quad (4)$$

Hence, the golden-ratio-parameterized self-similar equation likely represents a special 'design' that allows precisely 100% negative-feedback corrections for any ancestral deviations. Using simulations, we confirmed that φ = 0.618 yields asymptotic zero net noise accumulation, whereas smaller or larger values result in failed noise control by either insufficient suppression or over-correction, respectively (**Fig. 4g**). We further analyzed the perturbed RNAi or Env embryos, respectively, and found the estimated φ close to 0.618 (RNAi, φ = 0.614±0.0003; Env, φ = 0.603±0.001) (**Fig. 4h; Methods**), suggesting the robustness of the self-similar equation to perturbations. In addition, φ estimates remained consistently around 0.618 when using either 4-generation or 5-generation approximations, despite the narrower generation ranges and smaller sample sizes (**Fig. S14**).

Notably, the zero net noise represents a theoretical limit attained for infinite lineage length, and the $\alpha = \beta$ = 0.618 represents a population-level expectation. We derived the mathematically optimal φ that minimizes net noise and found it rapidly converges toward 0.618 as lineage length increases (**Supplementary Note III**); a lineage length of ~10-13 generations—matching the *C. elegans* embryogenesis—yields an optimal φ close to the golden ratio (**Fig. 4i**). Further evolutionary simulations showed that the golden ratio φ = 0.618 can emerge at the population level under natural selection for lineage length of 10 or 13 generations (**Fig. 4j and Fig. S14; Methods**). In line with this, in addition to estimating φ by pooling embryos within the same condition (control, RNAi, Env), we also performed individual-embryo-based estimation and found that although embryo-specific φ varied across individuals, they converged to the golden ratio when considered as a population in a meta-analysis (**Fig. 4k; Methods**). Finally, as one would expect, the self-similar equation of cell velocity also applies to cell displacement (**Fig. S14**), validating the velocity-based regulation of cell positions proposed in Fig. 3. Taken together, these results reveal a golden-ratio-parameterized self-similar equation governing the cell velocity conservation along developmental lineages, which secures the morphogenetic reproducibility of *C. elegans*.

Violation of the self-similar equation predicts hatching failure and reveals underlying genes

We next asked what would happen if the self-similar equation were violated. In *C. elegans*, embryogenesis begins with a single zygote and culminates at a stage composed of 558 cells that subsequently hatches[41]. For the 2,039 embryos analyzed in this study, we recorded lineage-resolved single-cell spatiotemporal features from 4-cell stage to ~350-cell stage, together with the final hatching outcome, classified as hatched (n = 1,930) or lethal (n = 109) (**Fig. 5a and Table S5**). It was unclear how violation of the self-similar kinematic equation could predict the hatching outcome.

To address this question, we applied the self-similar equation to the three-generation trio data in each embryo to predict the velocity behavior of each granddaughter cell in each trio and calculated the mean absolute error (MAE) for each embryo as a quantitative measure of deviation from the equation (**Methods**). Embryos that failed to hatch exhibited significantly larger MAE values, indicating stronger violation of the equation (**Fig. 5b**). Using MAEs of three coordinates as predictors in a logistic regression model yielded an area under the ROC curve (AUC) of approximately 0.89, demonstrating strong predictive power for hatching lethality (**Fig. 5c; Methods**). As a control, shuffling hatching outcomes among the embryos resulted in an AUC close to 0.5 (= 0.55), indicating that the observed predictive performance could not be explained by class imbalance or technical artifacts (**Fig. S15**).

The strong association between deviation from the self-similar equation and hatching lethality enabled the identification of genes required to maintain this equation. For each perturbed embryo, we calculated the Z-score of its MAE relative to control embryos and assessed statistical significance after multiple-testing correction (**Methods**). A gene was defined as required for maintaining the equation if its perturbation caused significant deviation in at least two replicate embryos and across at least two spatial coordinates. We applied these criteria to the ~2000 RNAi embryos covering ~700 genes and identified 24 candidate genes (**Fig. 5d**). Gene enrichment analysis revealed that these genes were significantly enriched for functions related to cytoskeleton organization, including components of motor protein complexes such as the kinesin complex (**Fig. 5d**). These results suggest that cytoskeletal regulation plays a central role in enforcing the self-similar equation and, consequently, in suppressing the propagation of positional noise during embryogenesis. This discovery is consistent with previous studies highlighting the critical roles of the cytoskeleton in cell polarity, cell migration and morphogenesis[59,60].

Discussion

In this study we demonstrate that seemingly chaotic morphogenesis is governed by simple mathematical–physical rules in the nematode *C. elegans*. Specifically, by establishing a unified geometric representation system that enables quantitative characterization of Waddington's canalization landscape, we identify migration velocity as the primary cell kinematic variable regulating morphogenetic reproducibility. As such, we transform an 80-year-old developmental metaphor into a mathematically defined entity, thereby providing a new mechanical framework for studying noise and noise control during development. Notably, a golden-ratio (φ)-parameterized self-similar equation describing cell velocity dynamics along developmental lineages represents, to our knowledge, the first kinematic conservation principle underlying animal morphogenesis. Functional analyses further show that developmental failure can be largely explained by violation of the self-similar equation, providing a quantitative framework linking cellular behaviors to developmental phenotypes, and that a cytoskeleton-enriched gene set is required to maintain this equation, offering concrete molecular entry points for dissecting the underlying molecular–cellular pathways. Our discovery of the self-similar equation also provides a unified framework bridging mother-daughter negative feedback and the long-standing "mother–sister similarity paradox" [61] that is also observed in our data (**Fig. S16**). Notably, the principles act on cell behavioral noise independently of specific morphogenetic trajectories, generating a natural conjecture that similar principles may also operate in embryogenesis of other organisms and in organogenesis of other organs.

Beyond these core discoveries, our results suggest a two-layer regulatory architecture underlying developmental robustness (**Fig. 6a**). The newly characterized layer - regulation of cell noise at the embryonic level - can be described by rather simple mathematical equations. Inspired by Koyck's transformation of the GDL model bridging micro- and macroeconomic processes[58], the microscopic self-similar equation (Eq. 3) can be rewritten as a macroscopic iterative form involving only two adjacent generations (t: daughter; t-1: mother), expressed as $\begin{cases} V_t^{new} = -\alpha V_t^{inherited} + \varepsilon \\ V_t^{inherited} = \beta\ (V_{t-1}^{new} + V_{t-1}^{inherited}) \end{cases}$, where V_t^{new} and $V_t^{inherited}$ represent the newly generated and inherited velocity determining factors (V-factors) in the daughter cell, and V_{t-1}^{new}

and $V_{t-1}^{inherited}$ represent the corresponding V-factors in the mother cell (**Supplementary Note IV**). This formulation provides a mechanistic interpretation of how the self-similar system may operate. Specifically, the newly generated V-factors in a daughter cell are determined by the total V-factors of its mother and directly contribute to velocity generation, rather than combining with the inherited component (**Fig. 6b**). Importantly, this iterative formulation also reveals mass conservation of V-factors. β denotes the fraction of V-factors inherited from the mother, whereas α denotes the fraction newly generated in the daughter relative to the inherited pool. When $\alpha = \beta = \varphi$ (0.618), the total amount of V-factors is conserved across successive generations, expressed as $\beta + \beta\alpha = 1$, or equivalently $1 - \beta = \beta\alpha$, indicating a constant turnover rate. Notably, the mass conservation condition $\beta + \beta\alpha = 1$ is mathematically equivalent to the limiting form of velocity conservation, $\alpha\beta / (1 - \beta) = 1$, derived from Eq. (4). The golden ratio $\varphi = 0.618$ thus uniquely satisfies both conservations under the constraint $\alpha = \beta$ which reflects an efficiency or energy constraint across two consecutive processes (**Supplementary Note V)**. Under this equivalence, the macroscopic iterative formulation defines the V-factor turnover as a molecular-level target of natural selection, while the microscopic GDL form defines embryonic net velocity noise as an embryonic-level target of selection. These deductions also showcase why and how the golden ratio can be selected by nature, enriching the general 'golden ratio biology'[62,63].

The broader significance of these results extends beyond developmental biology to general principles of dynamic systems. The GDL structure underlying our self-similar equation is a foundational framework in econometrics, first formulated by Koyck in 1954[58], for modeling dynamic adjustment with geometrically decaying memory. Beyond economics, the same distributed lag or autoregressive framework appears widely in neuroscience and biomedical engineering[64-66], physics and artificial intelligence[67,68], sustainability science and health policy[69,70], and signal processing and control engineering[71,72], where it governs memory, damping, and stability in linear or linearized dynamic systems. The observation that embryonic development follows a self-similar equation of this class, uniquely parameterized by the golden ratio, suggests that evolution may have selected an optimally stable dynamic regime to suppress lineage-level noise. This insight links developmental robustness to a general stability principle and provides a conceptual blueprint for designing robust dynamic systems in both biological and physical contexts.

References

1 Zhu, M. & Zernicka-Goetz, M. Principles of Self-Organization of the Mammalian Embryo. *Cell* **183**, 1467-1478 (2020). https://doi.org:10.1016/j.cell.2020.11.003

2 Scharloo, W. Canalization: genetic and developmental aspects. *Annual Review of Ecology and Systematics* **22**, 65-93 (1991).

3 Waddington, C. H. Canalization of development and the inheritance of acquired characteres. *Nature* **150**, 563-565 (1942).

4 Osterwalder, M. *et al.* Enhancer redundancy provides phenotypic robustness in mammalian development. *Nature* **554**, 239-243 (2018). https://doi.org:10.1038/nature25461

5 Karras, G. I. *et al.* HSP90 Shapes the Consequences of Human Genetic Variation. *Cell* **168**, 856-866 e812 (2017). https://doi.org:10.1016/j.cell.2017.01.023

6 Hornstein, E. & Shomron, N. Canalization of development by microRNAs. *Nat Genet* **38 Suppl**, S20-24 (2006). https://doi.org:10.1038/ng1803

7 Siegal, M. L. & Bergman, A. Waddington's canalization revisited: developmental stability and evolution. *Proc Natl Acad Sci U S A* **99**, 10528-10532 (2002). https://doi.org:10.1073/pnas.102303999

8 Mao, Y. & Wickstrom, S. A. Mechanical state transitions in the regulation of tissue form and function. *Nat Rev Mol Cell Biol* **25**, 654-670 (2024). https://doi.org:10.1038/s41580-024-00719-x

9 Mitchell, S. J., Pardo-Pastor, C., Tchoumakova, A., Zangle, T. A. & Rosenblatt, J. Energy deficiency selects crowded live epithelial cells for extrusion. *Nature* **646**, 1187-1194 (2025). https://doi.org:10.1038/s41586-025-09514-w

10 Zhang, Y., Cohen, O. Y., Moshe, M. & Sharon, E. Geometrically frustrated rose petals. *Science* **388**, 520-524 (2025). https://doi.org:10.1126/science.adt0672

11 Caldarelli, P. *et al.* Self-organized tissue mechanics underlie embryonic regulation. *Nature* **633**, 887-894 (2024). https://doi.org:10.1038/s41586-024-07934-8

12 Fabreges, D. *et al.* Temporal variability and cell mechanics control robustness in mammalian embryogenesis. *Science* **386**, eadh1145 (2024). https://doi.org:10.1126/science.adh1145

13 Firmin, J. *et al.* Mechanics of human embryo compaction. *Nature* **629**, 646-651 (2024). https://doi.org:10.1038/s41586-024-07351-x

14 Nelson, C. M. *et al.* Mechanobiology: Shaping the future of cellular form and function. *Cell* **187**, 2652-2656 (2024). https://doi.org:10.1016/j.cell.2024.04.006

15 Naganathan, S. R., Popovic, M. & Oates, A. C. Left-right symmetry of zebrafish embryos requires somite surface tension. *Nature* **605**, 516-521 (2022). https://doi.org:10.1038/s41586-022-04646-9

16 Guignard, L. *et al.* Contact area-dependent cell communication and the morphological invariance of ascidian embryogenesis. *Science* **369**, 158-+ (2020). https://doi.org:10.1126/science.aar5663

17 Saadaoui, M., Rocancourt, D., Roussel, J., Corson, F. & Gros, J. A tensile ring drives tissue flows to shape the gastrulating amniote embryo. *Science* **367**, 453-458 (2020). https://doi.org:10.1126/science.aaw1965

18 Collinet, C. & Lecuit, T. Programmed and self-organized flow of information during morphogenesis. *Nat Rev Mol Cell Biol* **22**, 245-265 (2021). https://doi.org:10.1038/s41580-020-00318-6

19 Negrete, J., Jr. & Oates, A. C. Towards a physical understanding of developmental patterning. *Nat Rev Genet* **22**, 518-531 (2021). https://doi.org:10.1038/s41576-021-00355-7

20 Villeneuve, C., McCreery, K. P. & Wickstrom, S. A. Measuring and manipulating mechanical forces during development. *Nature cell biology* **27**, 575-590 (2025). https://doi.org:10.1038/s41556-025-01632-x

21 Moghe, P. *et al.* Coupling of cell shape, matrix and tissue dynamics ensures embryonic patterning robustness. *Nature cell biology* **27**, 408-423 (2025). https://doi.org:10.1038/s41556-025-01618-9

22 Ishihara, K. *et al.* Topological morphogenesis of neuroepithelial organoids. *Nat Phys* **19**, 177-183 (2023). https://doi.org:10.1038/s41567-022-01822-6

23 Fernandez, P. A. *et al.* Surface-tension-induced budding drives alveologenesis in human mammary gland organoids. *Nat Phys* **17**, 1130-1136 (2021). https://doi.org:10.1038/s41567-021-01336-7

24 Shen, J., Liu, F. & Tang, C. Scaling dictates the decoder structure. *Sci Bull (Beijing)* **67**, 1486-1495 (2022). https://doi.org:10.1016/j.scib.2022.06.014

25 Chan, C. J. *et al.* Hydraulic control of mammalian embryo size and cell fate. *Nature* **571**, 112-116 (2019). https://doi.org:10.1038/s41586-019-1309-x

26 Gross, P. *et al.* Guiding self-organized pattern formation in cell polarity establishment. *Nat Phys* **15**, 293-300 (2019). https://doi.org:10.1038/s41567-018-0358-7

27 Hannezo, E. *et al.* A Unifying Theory of Branching Morphogenesis. *Cell* **171**, 242-255 e227 (2017). https://doi.org:10.1016/j.cell.2017.08.026

28 Atia, L. *et al.* Geometric constraints during epithelial jamming. *Nat Phys* **14**, 613-620 (2018). https://doi.org:10.1038/s41567-018-0089-9

29 Shah, G. *et al.* Multi-scale imaging and analysis identify pan-embryo cell dynamics of germlayer formation in zebrafish. *Nat Commun* **10**, 5753 (2019). https://doi.org:10.1038/s41467-019-13625-0

30 Xue, S. L., Yang, Q., Liberali, P. & Hannezo, E. Mechanochemical bistability of intestinal organoids enables robust morphogenesis. *Nat Phys* **21**, 608-617 (2025). https://doi.org:10.1038/s41567-025-02792-1

31 Hota, S. K. *et al.* Brahma safeguards canalization of cardiac mesoderm differentiation. *Nature* **602**, 129-134 (2022). https://doi.org:10.1038/s41586-021-04336-y

32 Xiao, L., Fan, D., Qi, H., Cong, Y. & Du, Z. Defect-buffering cellular plasticity increases robustness of metazoan embryogenesis. *Cell Syst* **13**, 615-630 e619 (2022). https://doi.org:10.1016/j.cels.2022.07.001

33 Yang, Q. *et al.* Cell fate coordinates mechano-osmotic forces in intestinal crypt formation. *Nature cell biology* **23**, 733-744 (2021). https://doi.org:10.1038/s41556-021-00700-2

34 Hoijman, E. *et al.* Cooperative epithelial phagocytosis enables error correction in the early embryo. *Nature* **590**, 618-623 (2021). https://doi.org:10.1038/s41586-021-03200-3

35 Tsai, T. Y. *et al.* An adhesion code ensures robust pattern formation during tissue morphogenesis. *Science* **370**, 113-116 (2020). https://doi.org:10.1126/science.aba6637

36 Priya, R. *et al.* Tension heterogeneity directs form and fate to pattern the myocardial wall. *Nature* **588**, 130-134 (2020). https://doi.org:10.1038/s41586-020-2946-9

37 Akieda, Y. *et al.* Cell competition corrects noisy Wnt morphogen gradients to achieve robust patterning in the zebrafish embryo. *Nature Communications* **10**, 4710 (2019). https://doi.org:10.1038/s41467-019-12609-4

38 Li, X. *et al.* Systems Properties and Spatiotemporal Regulation of Cell Position Variability during Embryogenesis. *Cell Rep* **26**, 313-321 e317 (2019). https://doi.org:10.1016/j.celrep.2018.12.052

39 Li, P. *et al.* Morphogen gradient reconstitution reveals Hedgehog pathway design principles. *Science* **360**, 543-548 (2018). https://doi.org:10.1126/science.aao0645

40 Xiong, F. *et al.* Interplay of cell shape and division orientation promotes robust morphogenesis of developing epithelia. *Cell* **159**, 415-427 (2014). https://doi.org:10.1016/j.cell.2014.09.007

41 Sulston, J. E., Schierenberg, E., White, J. G. & Thomson, J. N. The embryonic cell lineage of the nematode Caenorhabditis elegans. *Dev Biol* **100**, 64-119 (1983). https://doi.org:10.1016/0012-1606(83)90201-4

42 Cao, J. *et al.* Establishment of a morphological atlas of the Caenorhabditis elegans embryo using deep-learning-based 4D segmentation. *Nat Commun* **11**, 6254 (2020). https://doi.org:10.1038/s41467-020-19863-x

43 Du, Z., Santella, A., He, F., Tiongson, M. & Bao, Z. De novo inference of systems-level mechanistic models of development from live-imaging-based phenotype analysis. *Cell* **156**, 359-372 (2014). https://doi.org:10.1016/j.cell.2013.11.046

44 Richards, J. L., Zacharias, A. L., Walton, T., Burdick, J. T. & Murray, J. I. A quantitative model of normal Caenorhabditis elegans embryogenesis and its disruption after stress. *Dev Biol* **374**, 12-23 (2013). https://doi.org:10.1016/j.ydbio.2012.11.034

45 Moore, J. L., Du, Z. & Bao, Z. Systematic quantification of developmental phenotypes at single-cell resolution during embryogenesis. *Development* **140**, 3266-3274 (2013). https://doi.org:10.1242/dev.096040

46 Bao, Z., Zhao, Z., Boyle, T. J., Murray, J. I. & Waterston, R. H. Control of cell cycle timing during C. elegans embryogenesis. *Dev Biol* **318**, 65-72 (2008). https://doi.org:10.1016/j.ydbio.2008.02.054

47 Bao, Z. *et al.* Automated cell lineage tracing in Caenorhabditis elegans. *Proc Natl Acad Sci U S A* **103**, 2707-2712 (2006). https://doi.org:10.1073/pnas.0511111103

48 Lardennois, A. *et al.* An actin-based viscoplastic lock ensures progressive body-axis elongation. *Nature* **573**, 266-270 (2019). https://doi.org:10.1038/s41586-019-1509-4

49 Hubatsch, L. *et al.* A cell size threshold limits cell polarity and asymmetric division potential. *Nat Phys* **15**, 1075-1085 (2019). https://doi.org:10.1038/s41567-019-0601-x

50 Jordan, D. J. & Miska, E. A. Canalisation and plasticity on the developmental manifold of Caenorhabditis elegans. *Mol Syst Biol* **19**, e11835 (2023). https://doi.org:10.15252/msb.202311835

51 Kuang, X. *et al.* Computable early Caenorhabditis elegans embryo with a phase field model. *PLoS Comput Biol* **18**, e1009755 (2022). https://doi.org:10.1371/journal.pcbi.1009755

52 Du, Z. *et al.* The Regulatory Landscape of Lineage Differentiation in a Metazoan Embryo. *Dev Cell* **34**, 592-607 (2015). https://doi.org:10.1016/j.devcel.2015.07.014

53 Cinquin, A. *et al.* Semi-permeable Diffusion Barriers Enhance Patterning Robustness in the C. elegans Germline. *Dev Cell* **35**, 405-417 (2015). https://doi.org:10.1016/j.devcel.2015.10.027

54 Pohl, C. & Bao, Z. Chiral forces organize left-right patterning in C. elegans by uncoupling midline and anteroposterior axis. *Dev Cell* **19**, 402-412 (2010). https://doi.org:10.1016/j.devcel.2010.08.014

55 Campos, M. *et al.* A constant size extension drives bacterial cell size homeostasis. *Cell* **159**, 1433-1446 (2014). https://doi.org:10.1016/j.cell.2014.11.022

56 Tanouchi, Y. *et al.* A noisy linear map underlies oscillations in cell size and gene expression in bacteria. *Nature* **523**, 357-360 (2015). https://doi.org:10.1038/nature14562

57 Large, C. R. L. *et al.* Lineage-resolved analysis of embryonic gene expression evolution in C. elegans and C. briggsae. *Science* **388**, eadu8249 (2025). https://doi.org:10.1126/science.adu8249

58 Koyck, L. M. *Distributed Lags and Investment Analysis*. (North-Holland, 1954).

59 Lim, H. Y. G. & Plachta, N. Cytoskeletal control of early mammalian development. *Nat Rev Mol Cell Biol* **22**, 548-562 (2021). https://doi.org:10.1038/s41580-021-00363-9

60 SenGupta, S., Parent, C. A. & Bear, J. E. The principles of directed cell migration. *Nat Rev Mol Cell Biol* **22**, 529-547 (2021). https://doi.org:10.1038/s41580-021-00366-6

61 Sandler, O. *et al.* Lineage correlations of single cell division time as a probe of cell-cycle dynamics. *Nature* **519**, 468-471 (2015). https://doi.org:10.1038/nature14318

62 Naini, F. B. The golden ratio-dispelling the myth. *Maxillofac Plast Reconstr Surg* **46**, 2 (2024). https://doi.org:10.1186/s40902-024-00411-2

63 Rizzo, A. The Golden Ratio Theorem: A Framework for Interchangeability and Self-Similarity in Complex Systems. *Advances in Pure Mathematics* **13**, 559-596 (2023). https://doi.org:10.4236/apm.2023.139038

64 Nozari, E. *et al.* Macroscopic resting-state brain dynamics are best described by linear models. *Nat Biomed Eng* **8**, 68-84 (2024). https://doi.org:10.1038/s41551-023-01117-y

65 Urai, A. E. Structure uncovered: understanding temporal variability in perceptual decision-making. *Trends Cogn Sci* **30**, 54-65 (2026). https://doi.org:10.1016/j.tics.2025.06.003

66 Blanco-Duque, C. *et al.* Oscillatory-Quality of sleep spindles links brain state with sleep regulation and function. *Sci Adv* **10**, eadn6247 (2024). https://doi.org:10.1126/sciadv.adn6247

67 Lutsker, G. *et al.* A foundation model for continuous glucose monitoring data. *Nature* (2026). https://doi.org:10.1038/s41586-025-09925-9

68 Sobral, J. A., Perle, M. & Scheurer, M. S. Physics-informed transformers for electronic quantum states. *Nat Commun* **16**, 10811 (2025). https://doi.org:10.1038/s41467-025-66844-z

69 Liao, S. *et al.* Temperature-related hospitalization burden under climate change. *Nature* **644**, 960-968 (2025). https://doi.org:10.1038/s41586-025-09352-w

70 Fisman, D. N., Tuite, A. R. & Brown, K. A. Impact of El Niño Southern Oscillation on infectious disease hospitalization risk in the United States. *Proceedings of the National Academy of Sciences* **113**, 14589-14594 (2016). https://doi.org:10.1073/pnas.1604980113

71 Chen, G. Y., Gan, M., Wang, S. & Chen, C. L. P. Insights Into Algorithms for Separable Nonlinear Least Squares Problems. *IEEE transactions on image processing : a publication of the IEEE Signal Processing Society* **30**, 1207-1218 (2021). https://doi.org:10.1109/tip.2020.3043087

72 Olivari, M., Nieuwenhuizen, F. M., Venrooij, J., Bülthoff, H. H. & Pollini, L. Methods for Multiloop Identification of Visual and Neuromuscular Pilot Responses. *IEEE Trans Cybern* **45**, 2780-2791 (2015). https://doi.org:10.1109/tcyb.2014.2384525

73 Hutcheon, J. A., Chiolero, A. & Hanley, J. A. Random measurement error and regression dilution bias. *Bmj* **340**, c2289 (2010). https://doi.org:10.1136/bmj.c2289

74 Fitch, D. H. A. Evolution: An Ecological Context for C. elegans. *Current Biology* **15**, R655-R658 (2005). https://doi.org:https://doi.org/10.1016/j.cub.2005.08.028

75 Giri, S. *et al.* Evaluation of Daratumumab for the Treatment of Multiple Myeloma in Patients With High-risk Cytogenetic Factors: A Systematic Review and Meta-analysis. *JAMA Oncol* **6**, 1759-1765 (2020). https://doi.org:10.1001/jamaoncol.2020.4338

Data and Code Availability

The raw data, processed data and codes for this study can be accessible via the following GitHub repository: https://github.com/Jianguo-Wang/canalizationENV. The spatiotemporal data of RNAi and control embryos can be obtained from our previous study[32].

Methods

Single-cell-resolution spatiotemporal tracking of *C. elegans* embryos

Environmentally perturbed embryos. A total of 120 embryos were generated under environmentally perturbed conditions, comprising eight environmental categories and 40 distinct conditions, with three embryos per condition. Temperature perturbations (16°C, 18°C, 20°C, 22°C, and 24°C) applied during the 2–4 cell stage did not affect hatching. Similarly, heat shock treatments at 30°C for varying durations (10, 15, 20, 25, and 30 min) during the 2–4 cell stage resulted in normal hatching. To examine nutritional and metabolic perturbations, nematodes were cultured from the L1 larval stage for two consecutive generations on different bacterial food

sources (HB101, OP50, BW25113, HT115, and DA1877); all resulting embryos hatched normally. Supplementation with stearic acid (SA; 50–600 μg/mL) or glucose (GLU; 50–600 mM) from the L1 stage also produced normally hatched embryos, except at 600 mM glucose, which resulted in embryonic lethality. Similarly, culturing nematodes under varying sodium chloride (NaCl) concentrations (20–100 mM) did not affect hatching. Iron chloride ($FeCl_3$) treatments at concentrations of 1–8 mM applied at the L1 stage, as well as 8 mM at the L4 stage, yielded normally hatched embryos. In contrast, paraquat (PQ) treatments at concentrations of 1–8 mM applied at the L4 stage resulted in embryonic lethality in all cases. Among all environmentally perturbed embryos, 11 embryos (corresponding to five conditions) exhibited lethality at hatching and were successfully lineage-traced up to the 350-cell stage.

RNAi-perturbed and control embryos. RNAi and control embryos were generated as described in our previous study. Worms were cultured under standard laboratory conditions at 21°C unless otherwise specified. We focused on protein-coding genes with human orthologs located on chromosome I, as annotated in the Ensembl database. Gene expression data at the 4-cell, proliferative, and gastrulation stages were obtained from the EBI Expression Atlas generated by the modENCODE project. Genes with expression levels exceeding 5 transcripts per million (TPM) at any stage were retained, yielding 922 candidate genes. RNAi clone accuracy was verified by sequencing 752 expressed genes from the Ahringer RNAi library. RNAi was administered via the feeding method with minor modifications. Briefly, synchronized L1 larvae (20–25 worms per experiment) were transferred to RNAi plates seeded with bacteria expressing gene-specific double-stranded RNA and incubated for 36–48 h at 21°C. Embryos collected from treated worms were used for imaging. For genes causing severe defects such as larval lethality or sterility, a weaker RNAi treatment was applied at the L3–L4 stage. A total of 105 control embryos fed with bacteria carrying the empty L4440 vector all hatched normally. Among RNAi-treated embryos, 98 embryos (corresponding to 63 genes) exhibited embryonic lethality at hatching and were successfully traced until the 350-cell stage.

3D time-lapse microscopic imaging. Live imaging was performed as described previously. Briefly, 3–4 gravid young adult worms were dissected in egg buffer on multi-test slides. Embryos prior to the 4-cell stage were selected and transferred onto coverslips coated with polystyrene microspheres. A second coverslip was placed on top, and the chamber was sealed with Vaseline. Imaging was conducted using a spinning-disk confocal microscope (Revolution

XD) equipped with 488-nm (GFP) and 561-nm (mCherry) channels, controlled by MetaMorph software. Images were acquired using a 60× oil objective at 21°C for 4.75–6 h, with 75-s intervals and 30 Z planes at 1-μm spacing per channel. Imaging parameters were optimized to minimize photobleaching and phototoxicity while maintaining high signal-to-noise ratios. Hatching outcomes were assessed 24 h post-imaging. Of the imaged wild-type embryos, 304 out of 308 (98.7%) hatched normally without detectable morphological abnormalities, comparable to standard NGM culture conditions, indicating minimal imaging-induced perturbation.

Cell lineage reconstruction and extraction of spatiotemporal features. Cell lineages were reconstructed from 3D time-lapse image series using StarryNite software, following established protocols. Nuclei were automatically detected from histone::mCherry signals using hybrid blob-slice detection algorithms and subsequently tracked over time via semilocal neighborhood-based algorithms. Each cell was assigned a unique identity according to Sulston's nomenclature. Lineages were traced up to the 350-cell stage unless severe developmental defects prevented further progression. The reconstructed lineage data provided single-cell-resolution 4D spatiotemporal features consisting of developmental timing (including birth and division timings) and positioning (3D positions at each time point). Three types of lineage errors—early termination, excessive length, and excrescent branching—were manually identified and corrected. Multiple rounds of manual curation were performed using AceTree software. Lineage accuracy was assessed by examining 378 randomly selected terminal cells from 50 control embryos; only one tracing error was detected, yielding an overall accuracy of 99.9%. Residual errors were minimal and did not affect the conclusions of this study.

Aligning 4D features of different embryos into a unified geometric representation system

The goal of this study is to quantitatively characterize developmental canals by modeling relationships between mother–daughter cells, uncovering quantitative mathematical rules common for different cells along lineages within and across embryos, linking cellular features to organismal phenotypes. Accurate alignment of cell features (CCL: the time interval between two consecutive cell divisions; x, y and z coordinates) across embryos is therefore essential, given variation in overall developmental duration, embryo size and embryo orientation in culture.

Alignment of cell cycle lengths among embryos. (1) Scaling. Embryos exhibited variability in overall developmental pace, reflected by systematic differences in CCL. To quantify this variation, we estimated a scaling factor (SF) for each embryo relative to a reference embryo (ctr-emb58). The SF was defined as the slope obtained from passing-origin orthogonal regression between the CCLs of the reference embryo (independent variable) and those of the focal embryo (dependent variable). Raw CCLs were then multiplied by the reciprocal of the SF (1/SF) to obtain scaled CCLs. **(2) Evaluation of alignment quality.** Alignment quality was assessed using the Identity Score (IS), defined as the proportion of variance explained along the diagonal when plotting an embryo's CCLs against those of the reference embryo. Higher IS values indicate better alignment, although lower values may also reflect increased biological noise. **(3) Impact of reference selection.** To evaluate sensitivity to reference selection, SFs derived from ctr-emb58 were compared with those obtained using the average CCL profile of all control embryos as the reference. The strong linear correspondence between the two sets of SFs indicated that reference choice had minimal impact on alignment (Fig. S1).

Alignment of spatial coordinates via translation-rotation-scaling procedure. (1) Translation. For each embryo, the center of gravity was computed as the mean of all raw spatial coordinates. Translated coordinates were obtained by subtracting this center from each raw coordinate. **(2) Rotation.** Assuming comparable body axes across embryos, we treated the translated coordinates as linear transformations of a common Cartesian coordinate system defined by the anterior–posterior (A–P), left–right (L–R), and dorsal–ventral (D–V) axes. Principal component analysis (PCA) was applied to recover these axes, with the first three principal components corresponding to A–P, L–R, and D–V axes, respectively. For atypical embryos with unconventional axis proportions, ctr-emb58 was used as a reference to ensure consistent axis assignment. The PCA-based transformation ensured orthogonality of the rotated coordinates. **(3) Scaling.** After translation and rotation, differences in embryo size along each axis were quantified using scaling factors estimated analogously to those for CCL, with ctr-emb58 as the reference. Rotated coordinates were multiplied by the corresponding scaling factors to yield scaled coordinates. **(4) Evaluation of alignment quality.** Alignment quality was evaluated in two ways. First, IS was computed for each coordinate, analogous to CCL alignment. Second, we assessed whether each coordinate (x, y, or z) of a focal embryo aligned primarily with the same coordinate of the reference embryo and remained largely independent of the other two coordinates, thereby

detecting potential misalignments. **(5) Impact of reference selection.** Scaling factors derived using ctr-emb58 were compared with those obtained using the average coordinates of all control embryos as the reference. The strong agreement between the two confirmed minimal dependence on reference choice (Fig. S2). **(6) Alignment at cell division.** Although analyses primarily focused on spatial features at cell birth, negative feedback regulation may operate continuously throughout the cell cycle. Therefore, spatial features at cell division were also aligned. To maintain a consistent Cartesian coordinate system, the translation vectors, rotation matrices, and scaling factors derived from birth-time alignment were applied directly to division-time coordinates.

Modeling mother–daughter negative feedback in positional noise transmission

Negative feedback model. The negative feedback model for positional features used in this study follows established frameworks described in previous work and is detailed in the section *"Modeling mother-daughter cell noise transmission"* in the main text. Here, we provide additional clarifications relevant to the present analyses. A coefficient $a < 1$indicates that a deviation of the mother cell from its expected position is attenuated in the daughter cell, reflecting negative feedback. Since $k = a - 1$, the condition $k < 0$ (equivalently $a < 1$) serves as the operational criterion for mother–daughter negative feedback. Accordingly, the statistical significance of k in Eq. (2) is directly determined by that of a in Eq. (1). More details are discussed in Supplementary Note I.

Randomized mother–daughter cell pairs. To exclude the possibility that consistently negative k values arise from data structure artifacts rather than genuine biological effects, we constructed pseudo mother–daughter (M–D) pairs by randomly shuffling daughter cells relative to their corresponding mother cells. This randomization disrupts true lineage relationships while preserving the marginal distributions of positional features.

Robustness to birth and division stages. We further extended the model to consider positional features of both mother and daughter cells at birth and at division. The model structure remains unchanged except that, when assessing noise transmission from mother division to daughter birth, the mother's positional feature at birth is replaced by that at division (i.e., $X_{\mathrm{M,division}} - X_{\mathrm{D,birth}}$). Analogous formulations were applied to the remaining combinations:

718 $X_{\mathrm{M,division}} - X_{\mathrm{D,division}}$and $X_{\mathrm{M,birth}} - X_{\mathrm{D,division}}$. Comparisons among these four combinations
719 revealed that longer temporal intervals between mother and daughter stages are associated with
720 stronger negative feedback. Although incomplete division records for cells in the final generation
721 may slightly overestimate k for some combinations, the relative ordering of interval lengths across
722 the four scenarios is preserved.

723 **Theoretical analysis of noise control through continuous negative-feedback canals.**
724 We analytically examined noise accumulation along a cell lineage under different feedback
725 regimes. Without loss of generality, we set $a_i^2 = 1 (k = 0)$ for all mother–daughter (M–D) pairs to
726 represent no feedback, $a_i^2 = 1.5$ (approximately $k = 0.22$) for positive feedback, and $a_i^2 =$
727 0.5(approximately $k = -0.29$) for negative feedback. Cell noise was generated recursively as $X_i =$
728 $a_{i-1}X_{i-1} + \varepsilon_i$, where ε_i follows a standard normal distribution. Noise accumulation was
729 quantified using the variance $Var(X_i)$ across generations. Under negative feedback,
730 $Var(X_i)$ increases with diminishing returns, illustrating how continuous negative-feedback
731 developmental canals constrain noise accumulation over developmental time (**Supplementary**
732 **Note I**).

733 **Analysis of potential confounding factors for *k* estimation**

734 **Variation of scaling factors.** Because scaling can either stretch or compress raw coordinates, we
735 examined whether negative k values could arise as artifacts of scaling. Embryos were grouped
736 into ranges based on their scaling factors (SFs), centered on the median SF and spanning from 10%
737 to 100%. Narrow SF ranges correspond to embryos with similar scales and thus minimal scaling-
738 induced distortion. Within these ranges, the estimated k values consistently remained negative,
739 indicating that the observed negative feedback is not driven by scaling effects.

740 **Outlier effects due to low alignment quality.** Extreme outliers may bias slope estimates
741 in linear regression, particularly in embryos with poor alignment quality. We therefore excluded
742 embryos with low alignment scores (IS ≤ 0.9), which removed only a small number of samples,
743 and re-estimated k. Although this filtering slightly reduced the magnitude of some k values, the
744 re-estimated values remained highly correlated with those obtained from the full dataset, indicating
745 robustness to outlier effects.

Dilution effect caused by measurement error. When the independent variable contains measurement error, the estimated slope is attenuated toward zero, a phenomenon known as the dilution effect. In this context, the relationship between the error-adjusted slope a^{adjusted} and the observed slope a^{observed} is $a^{\text{adjusted}} = a^{\text{observed}} \frac{\sigma^2}{\sigma^2 - \sigma^2_{\text{measure}}}$, where σ^2 denotes the variance of the mother-cell feature and $\sigma^2_{\text{measure}}$ the corresponding measurement error variance (MEV)[73]. MEVs were determined from the smallest measurement units (u = 1 pixel for raw x and y coordinates and 4.5 pixels for raw z coordinates). Assuming a uniform distribution $U(O-u, O+u)$, the MEV for each feature was calculated accordingly. MEVs for rotated and scaled coordinates were derived as linear combinations of raw-coordinate MEVs and adjusted by embryo-specific scaling factors. The final MEV for each feature was obtained as the average across embryos.

Lineage tracking error. To evaluate robustness to tracking errors, we introduced controlled errors into specific generations. For example, imposing a 5% error rate in the fourth generation involved randomly swapping daughter identities for 5% of mother cells and propagating these errors to subsequent generations. We then re-estimated k and quantified accuracy as the squared Pearson correlation between original and perturbed estimates. Even with error rates up to 10% per generation—far exceeding those observed in the RNAi data—accuracy remained high, demonstrating strong robustness to tracking errors.

Alignment procedure. The translation–rotation–scaling alignment used to recover embryonic body axes may itself be influenced by cell noise, particularly during PCA-based rotation. To assess its impact on k estimation, we performed simulations in which embryos with known theoretical k values were subjected to the reverse procedure (scaling–rotation–translation) followed by the standard alignment pipeline. The resulting k estimates were highly correlated with the theoretical values, indicating that the alignment procedure does not introduce systematic directional bias comparable to dilution effects.

The $\sigma_D/\sigma_M < 1$ issue. In ordinary linear regression, the slope satisfies $a = (\sigma_D/\sigma_M)R$, where σ_D and σ_M are the standard deviations of daughter and mother cells, respectively, and R is Pearson's correlation coefficient. If $\sigma_D/\sigma_M < 1$ were universally true, a would necessarily be less than 1, potentially producing spurious negative k values. However, we found that σ_D and σ_M are generally comparable, and that the ratio σ_D/σ_M explains only part of the variance in k, indicating that the observed negative feedback cannot be attributed solely to this effect.

Simulating embryogenesis without negative feedback: null model of noise transmission

Quantifying expected cell noise variance. To assess the efficacy of developmental canals, we calculated both observed and expected positional noise variances for a representative seven-cell lineage across embryos. Observed variance was obtained directly from measured cell noises. Expected variance was computed by first extracting mother-independent noise terms (ε) using Eqs. (1, 2) and then cumulatively summing these variances along the lineage. For 4th-generation cells, the initial recorded generation, the expected variance was set equal to the observed variance.

Simulating embryogenetic process without negative feedback. Expected cell position noises within an embryo were generated by adding the expected noise of each mother cell to the mother-independent noise ε, with 4th-generation cells initialized using their observed noise values. This formulation assumes complete inheritance of mother-cell noise. Finally, expected cell noises were added to the mean cell positions observed across embryos to generate the expected spatial configurations.

Characterizing kinematic parameters underlying negative feedback in cell positioning

Displacement, velocity and time. Start and end positions were defined as the positional coordinates of the mother and daughter cells, respectively, using the embryo's center of mass as the origin. Because displacement equals migration time multiplied by velocity, reduced displacement may result from either shorter migration time or lower migration velocity. Thus, when a cell's start position exceeds its expected value, developmental regulation is expected to reduce migration time or velocity to ensure a robust end position. To identify the physical basis of mother–daughter negative feedback, we examined correlations between start position and both migration time and migration velocity. Migration time was defined as the interval between mother-cell division and daughter-cell division (i.e., scaled CCL). Migration velocity was calculated as relative displacement divided by migration time. A significantly negative correlation between start position and migration time indicates migration-time-based regulation, whereas a significantly negative correlation with migration velocity suggests migration-velocity-based modulation as the primary mechanism.

Distance, speed and time. In the main text, displacement and velocity were treated as vectors to preserve directionality, whereas distance and speed were calculated as scalar quantities.

Interpretation of start-position effects depends on the relative positions of mother and daughter cells. When the mother's start position is smaller than the daughter's position, a larger start position is expected to reduce migration time or speed. Conversely, when the mother's start position exceeds the daughter's position, a larger start position may correspond to increased migration time or speed. Migration distance was computed by summing distances between adjacent interpolated trajectory points from mother-cell division to daughter-cell division using time-lapse data. Linear interpolation standardized all cells to 11 common time points for comparability. To ensure consistent interpretation, the start position was refined relative to the expected end position: if the observed start position was smaller than the expected end position, the refined value was defined as their difference; otherwise, it was defined as the negative of that difference. Migration speed was calculated as migration distance divided by migration time. Negative feedback via time or speed regulation was evaluated by correlating the refined start position with migration time and migration speed, respectively.

Velocity dynamics along developmental lineage

Velocity dynamics and lineage patterns. By analyzing multiple subsets of embryos, we found that cell velocity—similar to spatial position and cell-cycle length—exhibits a well-defined expected distribution across embryos. Accordingly, velocity for each cell in each embryo was standardized using the population-level distribution estimated from 105 control embryos before modeling lineage-level velocity dynamics. To characterize velocity dynamics along lineages, velocity changes between successive generations were classified as increases (P) or decreases (N), and lineage patterns such as PNPN and NPNP were defined. The frequencies of these patterns were quantified both in the representative embryo and across the entire dataset.

Autocorrelation analysis. Autocorrelation analysis was conducted for two purposes: (1) to determine whether negative feedback acts exclusively on mother–daughter pairs or also involves more distant progenitors; and (2) to assess how negative-feedback strength varies with increasing generation interval. Across the five generations analyzed, negative correlations consistently dominated, indicating continuous negative feedback between a cell and its ancestral lineage. Moreover, the proportion of negative feedback decayed exponentially with increasing generation

interval, suggesting that the influence of ancestral velocity deviations progressively weakens over developmental time.

The φ-parameterized self-similar velocity equation and parameter estimation

Self-similar velocity equation. These observations motivated the formulation of a self-similar negative-feedback model of velocity dynamics along cell lineages. Our modeling framework extends the classical Koyck GDL model with several modifications. First, the intercept was fixed at zero because all velocities were standardized to have zero expectation. Second, the first parameter (α) carries a negative sign, reflecting negative feedback that dampens velocity deviations rather than amplifies them, thereby modeling a damping system rather than an inertial one. Third, whereas the Koyck model employs an infinite series to approximate long-term effects, we used a finite number of generations consistent with embryonic development from a zygote. Fourth, while the Koyck model is traditionally applied to a time series of a single variable, we extended it to the tree-structured lineage framework inherent to embryogenesis.

Estimating φ through pooling all trios from embryos within each condition. To estimate model parameters, we used a three-generation approximation of the GDL model. Ordinary least squares (OLS) regression was first applied for exploratory analysis, followed by nonlinear least squares (NLS) to estimate the unique parameter φ under the constraint $\alpha = \beta$ and to compare predictions from OLS and NLS. In the OLS framework, we estimated the coefficients $\theta_1 = -\alpha\beta$ and $\theta_2 = -\alpha\beta^2$ corresponding to V_{t-1} and V_{t-2}, respectively, and inferred α and β from their ratio. In the NLS framework, we directly estimated the single parameter φ under the constraint $\alpha = \beta = \varphi$. To examine the robustness of φ estimation under mild genetic or environmental perturbations, φ was further estimated in RNAi and Env embryos using the same procedure. During estimation, embryos with recorded hatching lethality were excluded, which could suggest disruption of the self-similar equation and cause potential bias in estimation. As an intuitive exploratory analysis, OLS was applied only to the x-coordinate given its higher signal-to-noise ratio, avoiding inaccuracies from collinearity between consecutive generations, while NLS was used for accurate coefficient estimation.

Theoretical and numeric analysis for the along-lineage conservation of total velocity

Uniqueness of φ = golden ratio under infinite lineage length. We first analyzed the asymptotic behavior of the self-similar feedback system under infinite lineage length by examining the deterministic propagation of a single initial perturbation. This minimal setting isolates the cumulative effect of negative feedback without introducing stochastic variability across generations. A fixed initial deviation $V_0 = 1$ was propagated across generations according to the closed-form residual function derived from the cumulative negative-feedback kernel: $R_n(\varphi, V_0) = V_0\left(1 - \sum_{k=2}^{n+1}\varphi^k\right)$, where R_n denotes the residual deviation at generation n (with $R_0 = V_0$). Residual trajectories were compared under three representative φ values: a low value ($\varphi = 0.4$), the golden ratio $\varphi = (\sqrt{5}-1)/2 \approx 0.618$, and a high value ($\varphi = 0.8$). This analysis demonstrates that only φ equal to the golden ratio yields geometric convergence of the residual toward zero, achieving asymptotic cancellation of the initial perturbation. Values smaller than the golden ratio lead to under-correction, whereas larger values produce over-correction and oscillatory amplification.

Population-level simulations demonstrating zero-net noise under φ = golden ratio. To visualize this behavior over a biologically relevant developmental depth, simulations were performed for 11 generations (generation 0 to 10). The same deterministic residual function was applied to propagate deviations under each φ value. In addition to the single-perturbation case, we extended the analysis to a population context by sampling 400 independent initial deviations V_0 from a standard normal distribution. For each φ and each generation, residuals were computed deterministically using the same kernel. These simulations show that across generations, only φ equal to the golden ratio maintains residuals centered and progressively contracts their variance toward zero, demonstrating along-lineage conservation of total velocity under φ = golden ratio.

Optimization of φ = golden ratio under finite lineage length. To determine how finite lineage length influences the optimal φ, we derived an exact closed-form expression for the variance of the accumulated velocity deviation at the terminal cell under lineage depth n, without invoking asymptotic limits (**Supplementary Note III**). The exact variance function is: $V_n(\varphi) = \sigma^2\left[(n+1)A^2 + \frac{2A\varphi^2}{(1-\varphi)^2}(1-\varphi^{n+1}) + \frac{\varphi^4}{(1-\varphi)^2(1-\varphi^2)}(1-\varphi^{2(n+1)})\right]$, where $A(\varphi) = 1 - \frac{\varphi^2}{1-\varphi}$. This decomposition reveals two structurally distinct contributions: (i) a linear accumulation term, $(n+1)A(\varphi)^2$, representing residual ancestral noise not fully canceled by feedback, which grows

proportionally with lineage length; and (ii) two geometrically saturating correction terms, proportional to $1-\varphi^{n+1}$ and $1-\varphi^{2(n+1)}$, capturing the progressive effectiveness of multi-generation negative feedback. The geometric terms increase rapidly at small n but approach saturation as lineage length increases, whereas the linear term increasingly dominates sensitivity to φ. Because $A(\varphi)=0$ is uniquely satisfied at $\varphi=(\sqrt{5}-1)/2$, the golden ratio minimizes the coefficient of linear variance growth. Consequently, although the optimal φ depends on lineage length for small n, it converges rapidly toward the golden ratio as lineage depth increases, without requiring an infinite-lineage limit.

Numeric results of optimal φ rapidly converges with lineage length. To quantify this dependence numerically, we directly minimized the exact variance function $V_n(\varphi)$ for each finite lineage length n, with φ restricted to the biologically meaningful interval [0.2, 0.85] and σ^2 fixed to 1 without loss of generality. For each lineage length, one-dimensional bounded optimization was applied to identify the φ that minimized terminal variance, yielding both the optimal φ and the corresponding minimum variance. This procedure was repeated for lineage depths $n=1$ to 25, covering early embryonic stages and exceeding those observed in *C. elegans*. The results show that lineage lengths of approximately 10–13 generations—comparable to the longest developmental lineages in *C. elegans*—are sufficient to place the system near the global optimum defined by the golden ratio, indicating that the golden ratio emerges as a finite-lineage optimum dictated by the exact variance structure of the self-similar feedback system.

Evolutionary simulations for the evolution of φ = golden ratio.

To examine whether the φ = golden ratio can emerge at the population level under finite lineage length, we performed evolutionary simulations based on the self-similar velocity equation. Each simulated embryo followed a lineage of fixed length (lineage length = 10 or 13, matching that of *C. elegans* embryogenesis). Cell velocity deviation V_t at generation t was governed by the φ-embedded self-similar equation $V_t=-\varphi\sum_{i=1}^{t-1}\varphi^i V_{t-i}+\varepsilon_t$, where φ is the heritable regulatory parameter subjected to natural selection and ε_t is stochastic noise. Noise terms were drawn independently from a Gaussian distribution and applied repeatedly at all generations (s.d. = 0.1). For each candidate φ, developmental stability was evaluated by simulating multiple embryos subjected to independent noise realizations (# embryos = 400). Fitness was defined as an

exponentially decreasing function of the variance of accumulative velocity deviation at terminal cell across embryos (or net velocity deviation): $\mathrm{Fitness}(\varphi) \propto \exp(-s\mathrm{Var}(V_T))$, where V_T denotes accumulative velocity deviation at the terminal cell and s controls selection strength ($s = 10$). This variance-based criterion penalizes both incomplete correction at small φ and over-correction with sign reversals at large φ. Populations of φ values (population size = 300[74]) evolved over discrete selection generations (selection generation = 200). In each generation, φ values were sampled proportional to fitness, followed by bounded Gaussian mutation (s.d. = 0.01; φ constrained to [0.2, 0.85]). Across all settings, the population mean φ asymptotically converged toward the golden ratio (φ = 0.618), with convergence slightly closer at lineage length = 13 than at lineage length = 10.

Estimation of φ by meta-analysis across individual embryos

In addition to estimating φ using pooled trios from embryos within each condition, we further assessed robustness at the individual-embryo level. For each embryo, nonlinear least squares (NLS) was applied by jointly fitting the three coordinates to obtain an independent estimate of φ and its standard error. Embryo-specific estimates were first combined within each condition using inverse-variance weighting to obtain a fixed-effect estimate. To account for variability among embryos, random-effects meta-analysis was then performed. The between-embryo variance component (τ^2) was estimated using the DerSimonian–Laird method[75], and random-effects weights were calculated as $1/(SE^2 + \tau^2)$. The cross-embryo estimate and its 95% confidence interval were computed from these weights, and between-embryo heterogeneity was quantified using Cochran's Q statistic and I^2. Embryos with recorded hatching lethality phenotypes were excluded from this analysis. All analyses were conducted in R using the *nls* function together with custom scripts for meta-analysis.

Predicting hatching lethality and identifying genes based on the self-similar equation

Quantifying the deviation from self-similar equation. To quantify deviations from the φ-embedded self-similar equation at the embryo level, we applied the one-parameter, three-generation self-similar model to all three-generation trios within each embryo. Predicted velocities for granddaughter cells were obtained, and the mean absolute error (MAE) between predicted and observed velocities was calculated separately for the three spatial coordinates.

Predicting hatching lethality. To predict binary hatching lethality phenotypes, MAE values from all three coordinates were used as predictors. Embryos were randomly divided into a training set (70%) and a testing set (30%). A logistic regression model was trained on the training set, and prediction performance was evaluated in the testing set using the area under the ROC curve (AUC). To evaluate the influence of sample imbalance between lethal and hatched embryos, we also shuffled the phenotypes across embryos and conducted logistic regression to obtain AUC ≈ 0.5.

Identifying genes required for the self-similar equation. To identify genes required for maintaining the self-similar equation, MAE values for each coordinate were first transformed into Z-scores using the corresponding mean and standard error estimated from control embryos. P-values were computed under a standard normal distribution and adjusted for multiple testing using the Benjamini–Hochberg (BH) procedure. A gene was defined as a candidate for maintaining the self-similar equation if its RNAi perturbation caused significant deviation in at least two embryos and along at least two coordinate axes. Gene Ontology enrichment analysis was performed using the R package clusterProfiler, with a significance threshold of 0.05 and BH correction applied.

Declaration of interests

The authors declare no competing interests.

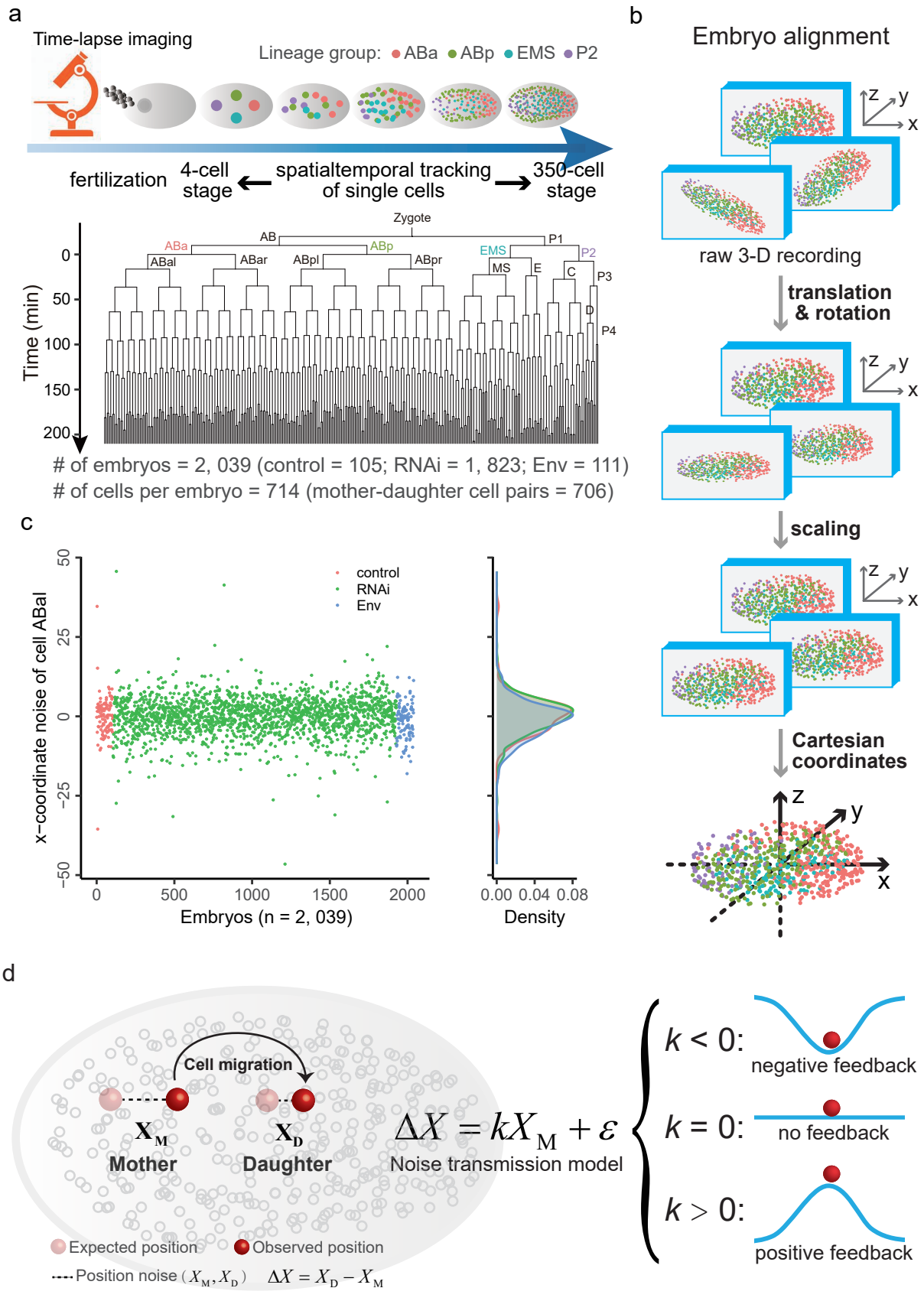

Fig. 1

Fig. 1. Summary of embryogenesis data and models for noise transmission

(a) Time-lapse microscopy was used to track single-cell spatiotemporal features during *C. elegans* embryogenesis, including cell cycle length (CCL) and three-dimensional positions (x, y, z), from the 4-cell to the 350-cell stage. A representative lineage tree is shown, with the time axis indicating division timing starting at the 4-cell stage. The corresponding spatial distribution of cells is displayed, with the four lineage groups (ABa, ABp, EMS, and P2, defined at the 4-cell stage) shown in distinct colors.

(b) Data-processing workflow. Raw 4D features (time and 3D position) were recorded for each embryo. Positional data were first translated to center the center of gravity at (0, 0, 0), then rotated to align the observed axes with consistent x-, y-, and z-axes corresponding approximately to the three body axes. A scaling procedure was applied to normalize overall embryonic duration and size. The aligned 4D features were then represented in a unified Cartesian coordinate system.

(c) Left, positional noise of an example cell (ABal) along the x coordinate across 2,039 embryos, with control, RNAi, and environmental (Env) embryos shown in different colors. Right, distribution of positional noise across all embryos.

(d) During migration from mother to daughter at any spatial coordinate, both cells deviate from their expected positions, defined as positional noise. This process was modeled in a unified framework in which X_M and X_D denote maternal and daughter positional noise, respectively. The change in noise is defined as $\Delta X = X_D - X_M$, and ε denotes daughter-specific noise independent of maternal noise. Three regulatory modes are characterized by slope k: negative feedback ($k < 0$, concave shape), no feedback ($k = 0$, flat shape), and positive feedback ($k > 0$, convex shape). Under negative feedback, daughter noise decreases relative to the mother; under no feedback, it remains unchanged; under positive feedback, it increases. Feedback regulation is therefore quantified by the sign of k.

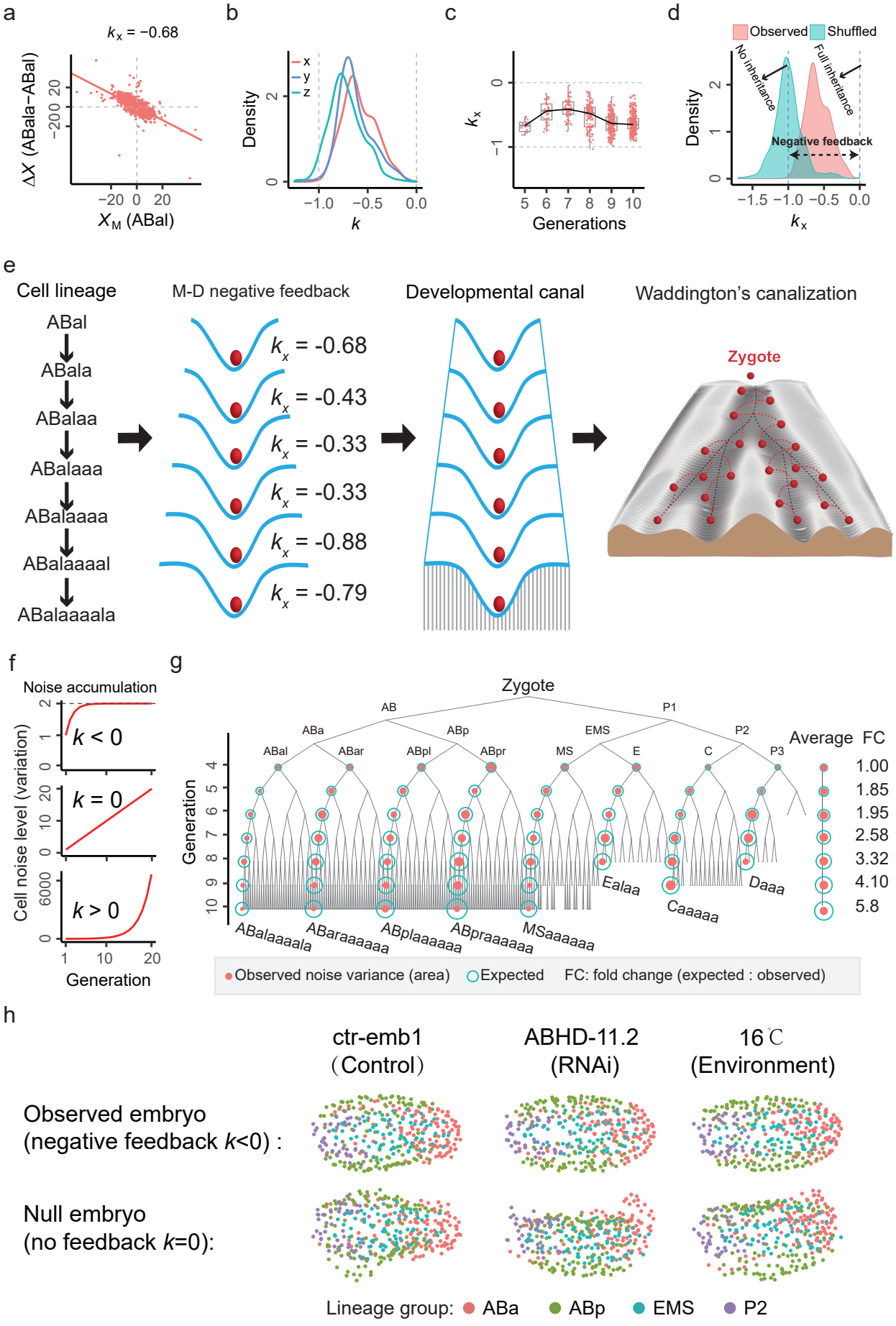

Fig. 2

Fig. 2. Mother–daughter negative feedbacks form continuous 'canals' that prevent positional noise propagation

(a) Scatter plot of X_{M} versus ΔX for an example mother–daughter (M–D) pair (mother: ABal; daughter: ABala) across 2,039 embryos. The regression slope ($k_{\mathrm{x}} = -0.68$) indicates negative feedback.

(b) Density distributions of k for all M–D pairs along the x, y, and z coordinates. Corresponding p-values are shown in Fig. S4.

(c) Variation of k across generations, revealing an hourglass-shaped pattern in which middle generations exhibit weaker negative-feedback strength.

(d) Pseudo M–D pairs generated by shuffling mothers and daughters were used to derive the null distribution of k. Shuffled pairs yielded $k \approx -1$, corresponding to no noise inheritance, whereas $k = 0$ indicates full noise inheritance. In contrast, real M–D pairs predominantly exhibit k values between −1 and 0, consistent with partial noise inheritance.

(e) A representative lineage annotated with corresponding k values. Concave canal segments (negative k) form continuous developmental canals that collectively constitute Waddington's canalization landscape.

(f) Theoretical accumulation of noise along a lineage under different feedback regimes. No feedback, positive feedback, and negative feedback are illustrated, respectively, assuming mother-independent noise (ε) follows a standard normal distribution (**Methods**). Noise variance increases without bound under no or positive feedback, whereas negative feedback constrains variance below an upper limit.

(g) Expected and observed noise variance across generations under the null model of full noise inheritance. Eight representative lineages are shown in different colors, with circle areas proportional to variance. Mean variance per generation and fold changes between expected and observed values are indicated.

(h) Three example embryos for each condition (control, RNAi and Env) illustrating predicted abnormalities under full noise inheritance (no feedback, $k = 0$), compared with their actual developmental outcomes under negative feedback.

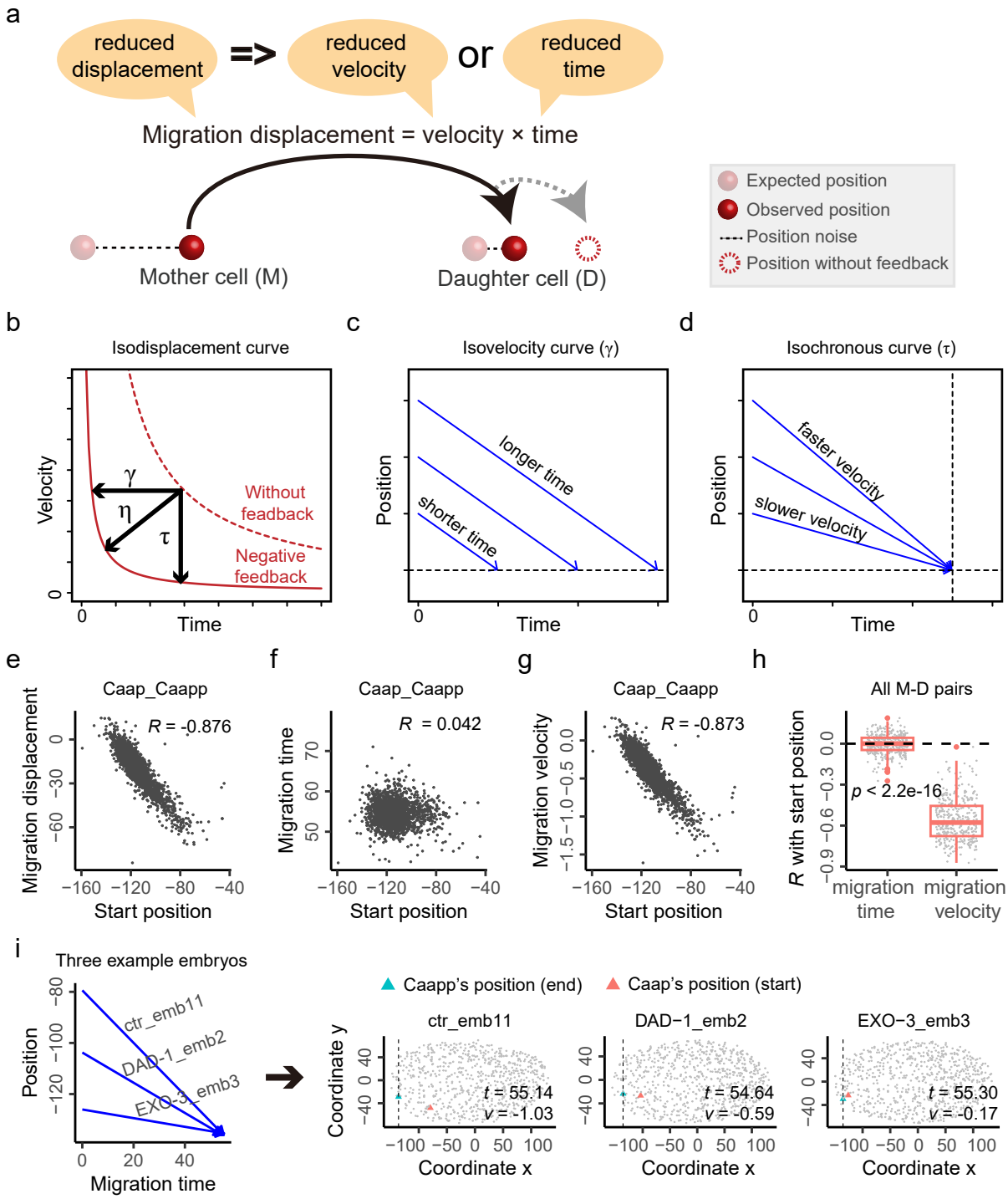

Fig. 3

Fig. 3. Positional negative feedback is achieved by regulating cell migration velocity

(a) Because daughter cells are born at the mother's position, identical migration displacement would yield identical positional noise in mother and daughter. Under negative feedback, daughter positional noise is reduced, implying smaller migration displacement. As displacement equals velocity × time, reduced displacement may result from reduced migration time, reduced migration velocity, or both.

(b) Theoretical framework illustrating three mechanisms of negative feedback on displacement: regulation of time (isovelocity regulation, γ), regulation of velocity (isochronous regulation, τ), or combined regulation (η).

(c) Expected time–position pattern under isovelocity regulation, producing parallel trajectories.

(d) Expected time–position pattern under isochronous regulation, producing convergent trajectories.

(e) Example mother–daughter (M–D) pair (Caap–Caapp) across embryos, showing a negative correlation between migration displacement and start position (x-coordinate position shown).

(f) Same data as in (e), plotting migration time versus start position, showing weak correlation.

(g) Same data as in (e), plotting migration velocity versus start position, showing a strong negative correlation.

(h) Pearson correlations between migration time or velocity and start position across all M–D pairs. A t-test indicates a significant difference, supporting migration velocity as the primary mechanism underlying negative feedback. The x-coordinate is shown here with y and z shown in Fig. S13.

(i) Same M–D pair as in (e), shown in three example embryos. Migration trajectories are indicated by arrows. Right, start and end positions are plotted in the embryonic x–y plane together with migration time and velocity.

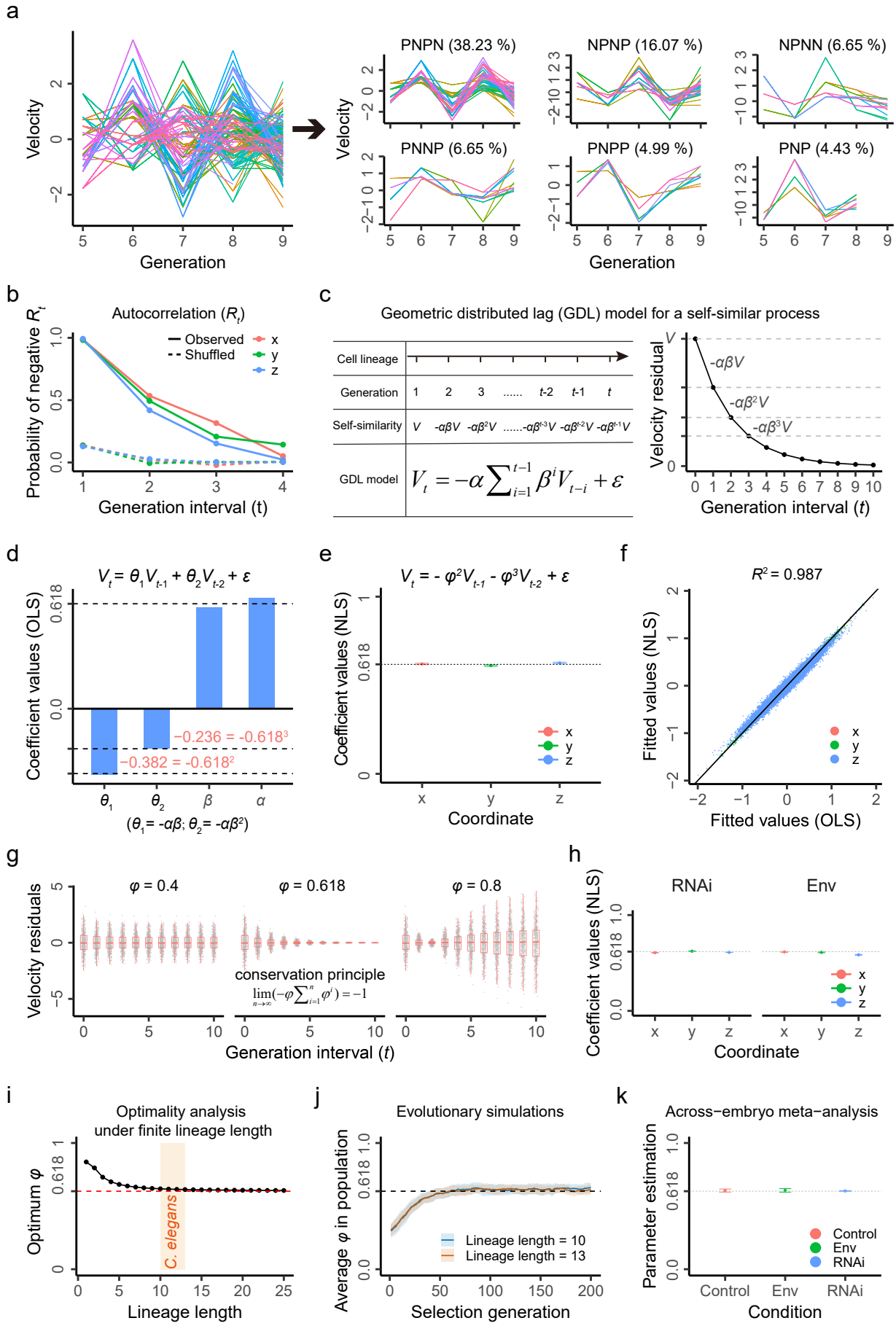

Fig. 4

Fig. 4. A φ-parameterized self-similar equation reveals an along-lineage velocity conservation principle

(a) Left, dynamics of cell velocity (Z-score) at the x coordinate across generations for all lineages in an example embryo (UNC-75_emb2). Right, the six most frequent lineage patterns in that embryo. "P" and "N" denote increases or decreases in velocity relative to the previous generation.

(b) Lineage-based autocorrelation analysis. R_t denotes the correlation between a cell and its progenitors separated by t generations. The proportion of negative feedback is calculated as (# negative R_t − # positive R_t)/N (N = 2,039 embryos). Exponential decay of this proportion indicates progressively diminishing ancestral effects.

(c) Hypothesized self-similar process in which velocity deviations are continuously counteracted by geometrically decaying negative feedback from progenitors. This process is modeled by a geometric distributed lag (GDL) model with parameters β (decay rate) and α (feedback strength).

(d) Ordinary least squares (OLS) estimation of the three-generation model using all mother–daughter–granddaughter trios from 105 control embryos. The model $V_t = \theta_1 V_{t-1} + \theta_2 V_{t-2} + \varepsilon$ is fitted to estimate θ_1 $(= -\alpha\beta)$ and θ_2 $(= -\alpha\beta^2)$, from which α and β are derived.

(e) Nonlinear least squares (NLS) estimation under the constraint $\alpha = \beta = \varphi$ using all trios from the 105 control embryos. The model $V_t = -\varphi^2 V_{t-1} - \varphi^3 V_{t-2} + \varepsilon$ is fitted at all three coordinates. Error bars indicate 95% confidence intervals. The combined estimate across coordinates is φ = 0.619±0.001 (φ ± s.e.).

(f) Comparison of OLS and NLS predictions. Near-perfect agreement indicates that the one-parameter constraint $\alpha = \beta = \varphi$ captures the underlying relationship.

(g) Simulation illustrating the theoretical consequences of different φ values in the GDL model. Only $\varphi = 0.618$ ensures exact counteraction of velocity deviations; smaller values yield insufficient suppression, whereas larger values cause overcorrection.

(h) NLS estimation of φ in RNAi and Env embryos followed the same procedure as in control embryos. Error bars indicate 95% confidence intervals. Combined estimates across coordinates are $\varphi = 0.614 \pm 0.0003$ for RNAi, and $\varphi = 0.603 \pm 0.001$ for Env.

(i) Theoretical and numerical analysis identifying the optimal φ that minimizes the variance of cumulative velocity deviation at the terminal cell as a function of lineage length. The shaded region indicates the lineage length of *C. elegans* embryogenesis (10–13 generations).

(j) Evolutionary simulations illustrating the emergence of the golden-ratio parameter φ under finite lineage length with stochastic noise introduced at all generations. Results for lineage lengths of 10 and 13 are shown.

(k) NLS estimation of φ is first conducted in individual embryos by combining the three coordinates into a single value per embryo, followed by meta-analysis to generate cross-embryo estimates for control, RNAi, and Env embryos, with 95% confidence intervals shown. The meta-analysis results are $\varphi = 0.623 \pm 0.006$ for control, $\varphi = 0.620 \pm 0.002$ for RNAi, and $\varphi = 0.625 \pm 0.007$ for Env.

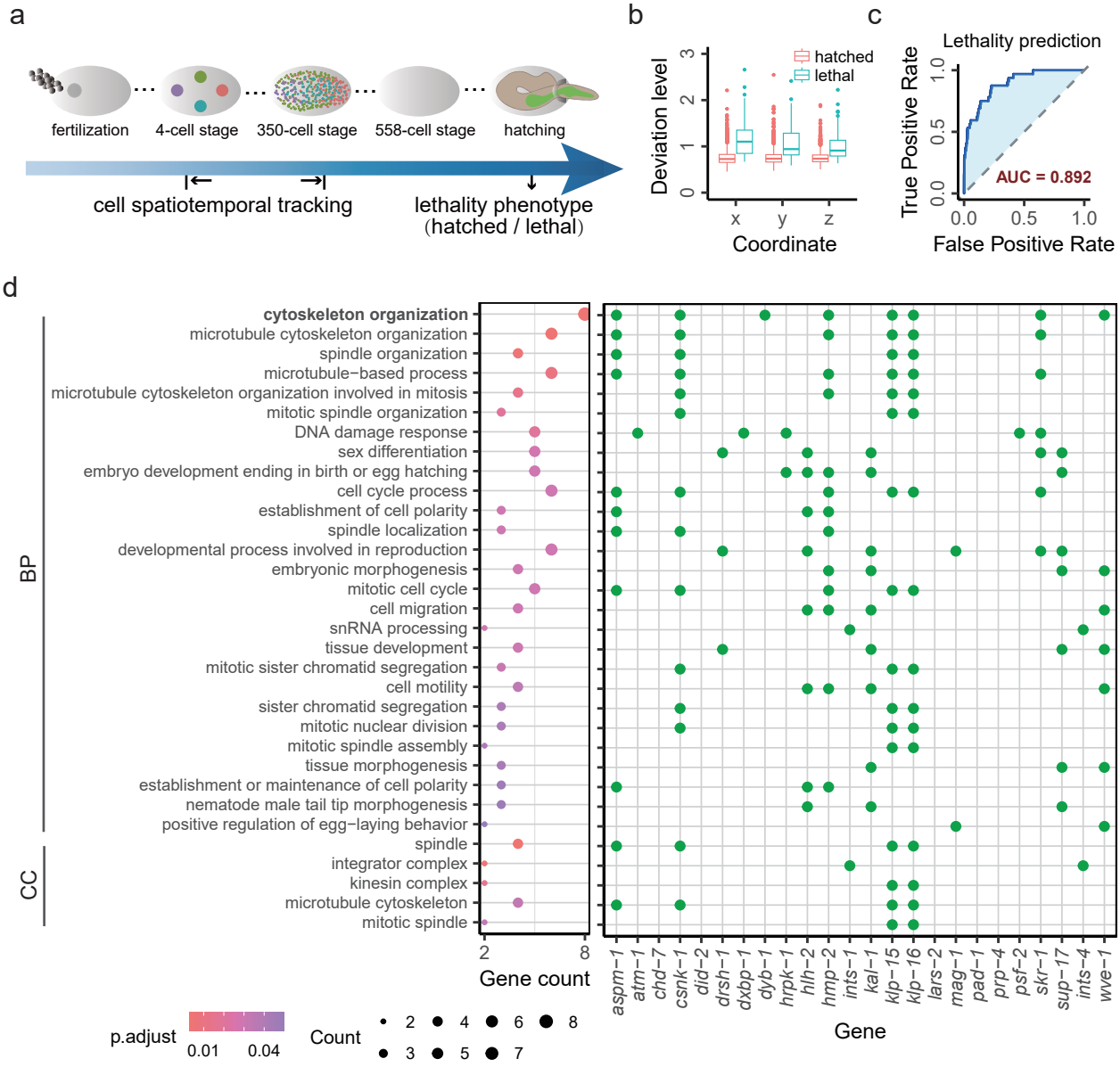

Fig. 5

Fig. 5. Violation of the self-similar equation predicts hatching failure and reveals underlying genes

(a) Embryos are lineage-traced from the 4-cell to the 350-cell stage, and hatching outcomes are recorded as hatched or lethal.

(b) Comparison of deviation from the self-similar equation between hatched and lethal embryos. The three-generation model with $\varphi = 0.618$ predicts granddaughter cells, and mean absolute error (MAE) quantifies deviation at the embryo level. Z-scores of MAEs based on control embryos are shown for the three coordinates.

(c) Logistic regression predicts hatching outcome using MAEs from the three coordinates as predictors. Seventy percent of embryos are used for training and the remainder for testing to calculate the AUC. A control analysis with shuffled outcomes is conducted to account for sample imbalance (Fig. S15).

(d) Candidate genes are defined as those whose RNAi causes significant deviation in at least two embryos and across at least two coordinate axes (one-tailed Z-test on MAEs, significance level = 0.05, with Benjamini-Hochberg correction). Gene ontology enrichment analysis is performed for biological process (BP), cellular component (CC), and molecular function (MF, not detected) at significance level = 0.05 with Benjamini-Hochberg correction.

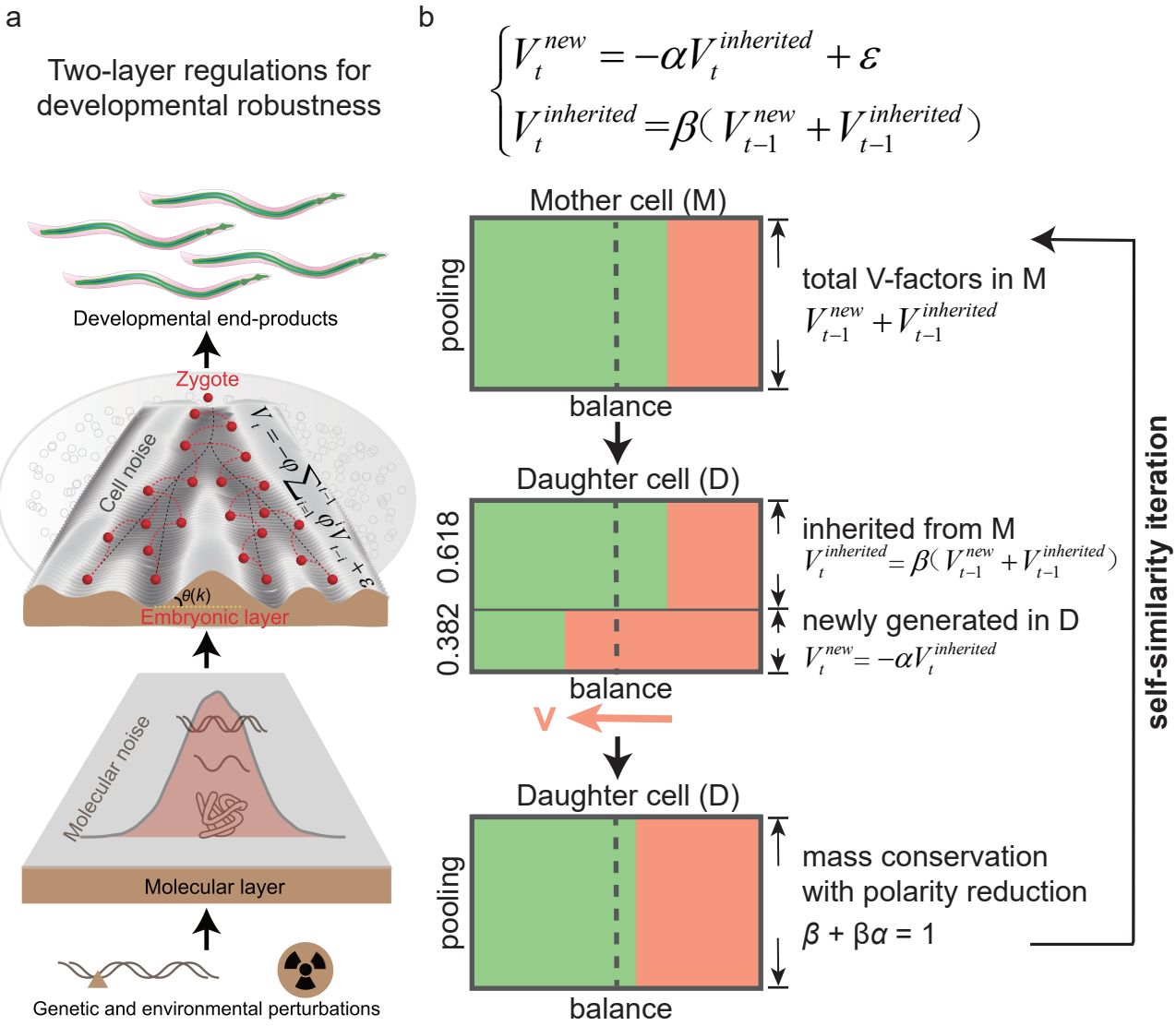

Fig. 6

Fig. 6. Two-layer regulatory architecture underlying developmental robustness and a working model for the self-similar velocity conservation equation

(a) Schematic of the two-layer regulatory architecture underlying developmental robustness. Embryonic-layer regulation is governed by the self-similar velocity equation.

(b) Schematic of the iterative formulation equivalent to the GDL-based self-similar velocity equation (Eq. 3). The iterative form involves only two adjacent generations. Velocity-determining factors (V-factors) in a cell have two states, corresponding to decreases or increases of cell velocity relative to the expected setting (green and orange). In the mother cell, V-factors represent overall polarity from unequal proportions of the two states. After division, maternal V-factors are transmitted to the daughter cell with a transmission rate $\beta = 0.618$. Newly generated V-factors in the daughter cell are produced at a generation rate $\alpha = 0.618$, yielding a proportion $\beta\alpha = 0.382$. These new V-factors have opposite polarity to inherited maternal V-factors and determine daughter cell velocity, with mass conservation imposed by $\beta + \beta\alpha = 1$. After one round of transmission and new generation, overall cellular V-factor polarity is reduced by pooling inherited and newly generated V-factors. This process iterates along the lineage, progressively driving cellular polarity toward zero and net velocity noise toward zero.